



Eidgenössische Technische Hochschule Zürich  
Swiss Federal Institute of Technology Zurich



Jialun Zhang

# Impact of Time Delays on Stability of Inertia-less Power Systems

Semester Thesis  
PSL 1806

EEH – Power Systems Laboratory  
Swiss Federal Institute of Technology (ETH) Zurich

Expert: Prof. Dr. Gabriela Hug  
Supervisors: M.Sc Uros Markovic

Zürich, August 15, 2018

# Abstract

Time delays appear in a variety of physical systems and their effects on stability have been investigated in areas like signal processing and circuit design. However, there has been little study on the effects of time delays on power system stability, which result in a system of Delay Differential Algebraic Equations (DDAE). As the number of converter-interfaced (renewable) generation increases, the impact of time delays coming from either local power electronics measurement or wide-area unit communication can play an important role in system stability.

This project aims to analyze the stability properties of inertia-less power systems with inclusion of various signal delays. The conventional mathematical representation of such systems, based on DAEs, will be extended to DDAEs, with the actual time delays adequately represented in the model. Subsequently, the stability margins will be assessed through Chebyshev discretization scheme and Padé approximants for both single and multiple (constant) time delays, as well as different system configurations. Furthermore, the participation factor and parameters sensitivity analysis have been conducted to identify the critical states and controller parameter. Meanwhile, both two-dimensional and three-dimensional bifurcation stability mapping has been implemented to visualize the impact of controller parameter variety towards critical time delay.

# Contents

<b>List of Acronyms</b>	<b>iv</b>
<b>List of Symbols</b>	<b>v</b>
<b>1 Introduction</b>	<b>1</b>
<b>2 Theoretical Analysis</b>	<b>3</b>
2.1 DDAE formulation . . . . .	3
2.2 Proposed approximation techniques . . . . .	5
2.2.1 Chebyshev discretization scheme . . . . .	5
2.2.2 Padé approximants . . . . .	7
<b>3 System Modelling</b>	<b>9</b>
3.1 VSC control scheme . . . . .	9
3.2 DDAE model . . . . .	12
3.2.1 Electrical system modeling . . . . .	12
3.2.2 Phase-Locked Loop . . . . .	12
3.2.3 Active Power Control . . . . .	13
3.2.4 Other DDAEs . . . . .	13
<b>4 Eigenvalue Spectrum Analysis</b>	<b>15</b>
4.1 Very small time-delay: DDAE vs. DAE . . . . .	15
4.2 Same time delay for all measurement signals . . . . .	16
4.3 Eigenvalue Analysis for Single Time Delay . . . . .	19
4.3.1 Single time delay: $e_g^\tau$ . . . . .	19
4.3.2 Single time delay: $i_g^\tau$ . . . . .	21
4.3.3 Single time delay: $i_s^\tau$ . . . . .	23
<b>5 Stability Mapping</b>	<b>27</b>
5.1 Participation factors . . . . .	27
5.2 Bifurcation analysis . . . . .	29
5.2.1 2-D bifurcation analysis . . . . .	29
5.2.2 3-D bifurcation analysis . . . . .	33

<i>CONTENTS</i>	iii
<b>6 Parameter Sensitivity Analysis</b>	<b>37</b>
<b>7 Conclusion &amp; Outlook</b>	<b>39</b>
<b>Bibliography</b>	<b>40</b>

# List of Acronyms

DAE	Differential Algebraic Equation
DDE	Delayed Differential Equation
DDAE	Delay Differential Algebraic Equation
PDE	Partial Differential Equations
VSC	Voltage Source Converter
DG	Distributed Generators
PE	Power Electronic
SMIB	Single-Machine Infinite-Bus
SM	Synchronous Machine
TSO	Transmission System Operator
PLL	Phase-Locked Loop
APC	Active Power Controller
VIE	Virtual Inertia Emulation
APDC	Active Power Droop Control
LPF	Low Pass Filter
RPC	Reactive Power Controller
SRF	Synchronously-rotating Reference Frame
PF	Participation Factor
PS	Parameter Sensitivity

# List of Symbols

## Unit Commitment Symbols

Symbol	Description
$f$	Differential equation
$g$	Algebraic equation
$x$	State variable
$x_\tau$	Delayed state variable
$y$	Algebraic variable
$y_\tau$	Delayed algebraic variable
$z$	Discrete event variable
$\tau$	Constant time delay
$\lambda$	Eigenvalue
$A_0$	Characteristic matrix
$I_n$	Identity matrix
$M$	Discretization matrix
$D_N$	Chebyshev differential matrix
$e_{g\tau}$	Delayed voltage measurement from primary side of transformer
$i_{g\tau}$	Delayed current measurement from primary side of transformer
$i_{s\tau}$	Delayed current measurement from converter
$p_{ki}$	Participation factor of $k^{th}$ state in $i^{th}$ mode
$l_k^i$	Element of $k^{th}$ element in $i^{th}$ left eigenvector matrix
$r_k^i$	Element of $k^{th}$ element in $i^{th}$ right eigenvector matrix
$a_{n,k}$	Sensitivity of $n^{th}$ mode to $k^{th}$ parameter

# List of Figures

2.1	Matrix M structure for a system with a single time delay [1] . . . . .	7
3.1	Original VSC control scheme. [2] . . . . .	9
3.2	Same time on three measurement signals. . . . .	10
3.3	Various time on three measurement signals. . . . .	10
4.1	Eigenvalues of DAE and DDAE using Chebyshev and Padé Approximation	16
4.2	Full eigenvalue spectrum computed using Padé approximation for time delay . . . . .	17
4.3	Full eigenvalue spectrum computed using Chebyshev discretization for time delay . . . . .	17
4.4	Critical eigenvalues computed using Padé approximation for time delay .	18
4.5	Critical eigenvalues computed using Chebyshev discretization for time delay	18
4.6	$e_g^\tau$ introduced in VSC control structure . . . . .	19
4.7	Single time delay introduced by $e_g^\tau$ ranging from 4200 to 4650 $\mu$ s . . . . .	20
4.8	Single time delay introduced by $e_g^\tau$ ranging from 4200 to 4650 $\mu$ s in a reduced range . . . . .	20
4.9	$i_g^\tau$ introduced in VSC control structure . . . . .	21
4.10	Single time delay introduced by $i_g^\tau$ ranging from 1400 to 1700 $\mu$ s . . . . .	22
4.11	Single time delay introduced by $i_g^\tau$ ranging from 1400 to 1700 $\mu$ s in a reduced range . . . . .	22
4.12	$i_s^\tau$ introduced in VSC control structure . . . . .	23
4.13	Single time delay introduced by $i_s^\tau$ ranging from 200 to 215 $\mu$ s . . . . .	23
4.14	Single time delay introduced by $i_s^\tau$ ranging from 200 to 215 $\mu$ s in a reduced range . . . . .	24
4.15	$\tau_{e_g}, \tau_{i_g}$ affect critical time-delay $\hat{\tau}_{i_s}$ . . . . .	25
4.16	APC in VIE mode applying to grid-frequency following case . . . . .	26
4.17	APC in Droop-based mode applying to grid-frequency forming case . . . .	26
5.1	Participation factors for $\hat{\lambda} = 3.5697 \pm j6913.8684$ . . . . .	28
5.2	Participation factors for $\hat{\lambda} = 23.9151 \pm j7677.1995$ . . . . .	28
5.3	Stability Map on $\hat{\tau} - K_p^v$ plane . . . . .	29
5.4	Stability Map on $\hat{\tau} - K_i^v$ plane . . . . .	30

5.5	Stability Map on $\hat{\tau} - K_f^i$ plane . . . . .	30
5.6	Stability Map on $\hat{\tau} - K_p^i$ plane . . . . .	31
5.7	Stability Map on $\hat{\tau} - K_i^i$ plane . . . . .	32
5.8	Stability Map on $\hat{\tau} - K_f^v$ plane . . . . .	32
5.9	Stability Map on $\hat{\tau} - H$ plane . . . . .	33
5.10	Stability Surface in the $\hat{\tau} - K_p^v - K_i^v$ , System is stable under shaded area	33
5.11	Stability Surface in the $\hat{\tau} - K_p^i - K_i^i$ , System is stable under shaded area	34
5.12	Stability Map on $\hat{\tau} - K_d - H$ plane . . . . .	35
5.13	Stability Map on $\hat{\tau} - D_p - D_q$ plane . . . . .	35
5.14	Stability Map on $\hat{\tau} - K_p^{pll} - K_i^{pll}$ plane . . . . .	36
6.1	Parameter Sensitivity for critical eigenvalue $\hat{\lambda} = 3.5697 \pm j6913.8684$ . . .	38
6.2	Parameter Sensitivity for critical eigenvalue $\hat{\lambda} = 23.9151 \pm j7677.1995$ . .	38



# List of Tables

4.1	Critical time delay for each case . . . . .	24
5.1	Critical time delay changes with various $K_p^v$ ( $10\mu s$ error) . . . . .	29
5.2	Critical time delay changes with various $K_i^v$ . . . . .	29
5.3	Critical time delay changes with various $K_f^i$ . . . . .	30
5.4	Critical time delay changes with various $K_p^i$ ( $10\mu s$ error) . . . . .	31
5.5	Critical time delay changes with various $K_i^i$ . . . . .	31
5.6	Critical time delay changes with various $K_f^v$ . . . . .	32

# Chapter 1

## Introduction

With the development of intermittent sources, an increasing amount of Distributed Generators has been applied to the current grid. The share of Power Electronic devices has grown dramatically in recent years. This trend has transformed the power generators from traditional generation sources such as synchronous machines towards Power Electronic (PE) interfaced and localized generators. Although more  $CO_2$  emissions could be avoided from the benefit of this trend as shown in [3], the power system, however, is now experiencing a low-inertia condition, resulting in detrimental consequences with respect to system stability margin [4]. As a result, a new concept called virtual inertia emulation has been evaluated in the literature [5–8], with the goal of reproducing the rotational inertia effect using PEs. A proper Voltage Source Converter (VSC) scheme has been proposed in all four papers.

Normally to analyze the stability of the power system, a widely implemented tool is small-signal analysis, which focuses on the stability at the equilibrium operation point after a disturbance. In [9] a low-inertia system has been analyzed through a small-signal method, whereas time delay signals occurring at power electronics are omitted. In [10] time delay signals are considered with further analysis through Padé Approximants method. However, the conclusions drawn from the adopted simplified Padé method may result in defective data. Research conducted in [11] has applied the Chebyshev Discretization scheme for studying a simplified VSC scheme without the consideration of Inner Loop Controller.

To encompass time delay signals into the existing mathematical modeling of the power system, a transition from Differential Algebraic Equation (DAE) to Delay Differential Algebraic Equations (DDAE) has to be formulated. A complete methodology and its derivation have been proposed in [12] which offers an insight into the DDAE formulation from existing DAE model. Additionally, [1] further addresses the transcendental nature of the characteristic matrix with four approximation approaches including both Chebyshev Discretization and Padé methods and compares the respective simulation results from a 1479 buses transmission system model. Due to the fact that both synchronous

machines and wind generators are analyzed in this research, it remains unclear what impact of VSC scheme renewable sources will impose on the stability of the system independently.

In this project, a complete DDAE model based on existing VSC control model in DAE form with the introduction of multiple measurement time delay signals is derived. Meanwhile, the critical eigenvalues (modes) are investigated through the research of eigenvalue spectrum. In addition, a participation factor analysis is applied to identify the critical states that contribute to the critical eigenvalues. Furthermore, a parameter sensitivity analysis is assessed for critical modes and bifurcation mappings regarding various controller parameters are displayed.

## Chapter 2

# Theoretical Analysis

### 2.1 DDAE formulation

As mentioned in the introduction, a small signal analysis is applied to analyze the dynamic stability of a system at a stationary working point. Normally, DAEs are formulated as a set of equations to describe the intrinsic stability behaviour. In this section, the derivation of the DAE model is presented, followed by the next section illustrating the derived DDAE model.

In [11] we see a very clear process that describes the derivation of a DDAE model from a DAE model. A concise derivation is also presented here for the sake of further clarification:

$$\begin{aligned}\dot{\mathbf{x}} &= \mathbf{f}(\mathbf{x}, \mathbf{y}, \mathbf{z}) \\ \mathbf{0} &= \mathbf{g}(\mathbf{x}, \mathbf{y}, \mathbf{z})\end{aligned}\tag{2.1}$$

Equation (2.1) describes the composition of the Differential Algebraic Equations. In this equation set,  $\mathbf{x}$  is the vector of state variables, while  $\mathbf{y}$  and  $\mathbf{z}$  are the vector of algebraic and discrete event variables respectively. In this project discrete event variables are beyond the scope of research and thus omitted in the following equations.  $\mathbf{f}$  and  $\mathbf{g}$  represents differential and algebraic equations respectively.

Yet the DAE model could not represent the effect brought by the time delay variables. Hence, a set of DDAEs has to be derived from the existing DAE model for further capturing the characteristics of the system. When we consider constant time delay signals  $\tau$  being introduced into the DAE form, we consequently obtain the following equations as:

$$\begin{aligned}\mathbf{x}_\tau &= \mathbf{x}(t - \tau) \\ \mathbf{y}_\tau &= \mathbf{y}(t - \tau)\end{aligned}\tag{2.2}$$

$$\begin{aligned}\dot{\mathbf{x}} &= \mathbf{f}(\mathbf{x}, \mathbf{y}, \mathbf{x}_\tau, \mathbf{y}_\tau, \mathbf{z}) \\ \mathbf{0} &= \mathbf{g}(\mathbf{x}, \mathbf{y}, \mathbf{x}_\tau, \mathbf{y}_\tau, \mathbf{z})\end{aligned}\tag{2.3}$$

From the general form of the DDAE model shown in (2.3), it is noticeable that both the state and algebraic variables are introduced with time delays. However, only algebraic variables introduced with time delayed signals are considered in differential equations. A reduced DDAE model (2.4) named index-1 Hessenberg form could be derived. As illustrated in [13], this form is sufficient to indicate the small-signal stability behaviour of the system.

$$\begin{aligned}\dot{\mathbf{x}} &= \mathbf{f}(\mathbf{x}, \mathbf{y}, \mathbf{x}_\tau, \mathbf{y}_\tau, \mathbf{z}) \\ \mathbf{0} &= \mathbf{g}(\mathbf{x}, \mathbf{y}, \mathbf{x}_\tau, \mathbf{z})\end{aligned}\tag{2.4}$$

Now assuming that the system is operating at a stationary point, the above reduced DDAE model could be linearized at this equilibrium solution which yields:

$$\begin{aligned}\Delta\dot{\mathbf{x}} &= \mathbf{f}_x\Delta\mathbf{x} + \mathbf{f}_{x_d}\Delta\mathbf{x}_d + \mathbf{f}_y\Delta\mathbf{y} + \mathbf{f}_{y_d}\Delta\mathbf{y}_d \\ \mathbf{0} &= \mathbf{g}_x\Delta\mathbf{x} + \mathbf{g}_{x_d}\Delta\mathbf{x}_d + \mathbf{g}_y\Delta\mathbf{y}\end{aligned}\tag{2.5}$$

If  $\mathbf{g}_y$  is non-singular, the above equations could be rewritten in the following form:

$$\dot{\mathbf{x}} = \mathbf{A}_0\mathbf{x}(t) + \sum_{i=1}^{\nu} \mathbf{A}_i\mathbf{x}_i(t - \tau_i)\tag{2.6}$$

with,

$$\mathbf{A}_0 = \mathbf{f}_x - \mathbf{f}_y\mathbf{g}_y^{-1}\mathbf{g}_x\tag{2.7}$$

$$\mathbf{A}_1 = \mathbf{f}_{x_\tau} - \mathbf{f}_y\mathbf{g}_y^{-1}\mathbf{g}_{x_\tau} - \mathbf{f}_{y_\tau}\mathbf{g}_y^{-1}\mathbf{g}_x\tag{2.8}$$

This equation (2.6) is defined as linear delay differential equation (DDE).  $\mathbf{A}_0$  is the state matrix of the standard DAE matrix which is not varied with time-delay variables, whereas  $\mathbf{A}_1$  is the matrix containing the time-delay variables. When a sample solution  $\mathbf{x} = e^{st}\mathbf{v}$  proposed in [12] is substituted into the DDE, a final characteristic matrix could be obtained as:

$$\Delta(\lambda) = \lambda\mathbf{I}_n - \mathbf{A}_0 - \sum_{i=1}^{\nu} \mathbf{A}_i e^{-\lambda\tau_i}\tag{2.9}$$

Equation (2.9) is the characteristic matrix which captures the stability characteristics from its spectrum of roots [14]. When observing any positive root, the system is unstable and if all roots lie at the left-side of imaginary axis, the system is stable. However, if further observation is made, equation (2.9) appears to be transcendental, meaning that there is an infinite number of roots. Nonetheless, only rightmost eigenvalues are mostly considered for identifying the stability of the system. With three essential properties of the characteristic equation illustrated in [12], the right-side plane roots are supposed to

be finite. Hence, numerical approximation methods have to be implemented in order to approximate a subset of the full spectrum. In the next section, two techniques will be proposed with respect to the approximation of the results, providing a fundamental theoretical foundation for this project.

## 2.2 Proposed approximation techniques

In this section, two approximation methods are introduced. The first one is Chebyshev discretization scheme, which can be applied to both small and large time delays. The second one is Padé approximation method, normally used for small time delays [1]. Since the time delays related to local measurement in power electronics vary from microseconds ( $\mu\text{s}$ ) to milliseconds ( $\text{ms}$ ), both techniques could be implemented. A mathematical formulation of both techniques is conducted in the following part.

### 2.2.1 Chebyshev discretization scheme

To address the transcendental nature of the characteristic matrix (2.9), [1] proposes an approach to transform the original computation of DDE eigenvalues into calculating roots of infinite dimension Partial Differential Equations (PDE) system. This process keeps the information needed for the stability analysis. The benefit of this transformation is that the PDE system solutions are tractable with the employment of finite element discretization approach.

When only state time-delay variables are considered, an additionally simplified form of the Hessenberg DDAE model could be created:

$$\begin{aligned}\dot{\mathbf{x}} &= \mathbf{f}(\mathbf{x}, \mathbf{y}, \mathbf{x}_\tau) \\ \mathbf{0} &= \mathbf{g}(\mathbf{x}, \mathbf{y}, \mathbf{x}_\tau)\end{aligned}\tag{2.10}$$

Repeating the previous procedure, the final form of the characteristic matrix with only a single time-delay becomes:

$$\Delta(\lambda) = \lambda \mathbf{I}_n - \mathbf{A}_0 - \mathbf{A}_1 e^{-\lambda\tau}\tag{2.11}$$

where,

$$\mathbf{A}_0 = \mathbf{f}_x - \mathbf{f}_y \mathbf{g}_y^{-1} \mathbf{g}_x\tag{2.12}$$

$$\mathbf{A}_1 = \mathbf{f}_{x_\tau} - \mathbf{f}_y \mathbf{g}_y^{-1} \mathbf{g}_{x_\tau}\tag{2.13}$$

Applying a finite element method, discretization matrix  $\mathbf{M}$  can be derived:

$$\mathbf{M} = \begin{bmatrix} \hat{\mathbf{C}} \otimes \mathbf{I}_n & & \\ \mathbf{A}_1 & \mathbf{0} & \dots & \mathbf{0} & \mathbf{A}_0 \end{bmatrix} \quad (2.14)$$

Here  $\otimes$  represents the Kronecker product and  $\hat{\mathbf{C}}$  indicates the  $N - 1$  rows of matrix  $\mathbf{C}$ :

$$\mathbf{C} = -2\mathbf{D}_N/\tau \quad (2.15)$$

$\mathbf{D}_N$  is the Chebyshev differential matrix of dimensions  $(N + 1) \times (N + 1)$ . This matrix is used to interpolate the discretization points in the range  $[-1, 1]$ , defined through Chebyshev nodes as follows:

$$x_k = \cos\left(\frac{k\pi}{N}\right), \quad k = 0, \dots, N. \quad (2.16)$$

Furthermore, these components composes the elements in the differentiation matrix numerically defined as:

$$\mathbf{D}_{(i,j)} = \begin{cases} \frac{c_i(-1)^{i+j}}{c_j(x_i - x_j)}, & i \neq j \\ -\frac{1}{2} \frac{x_i}{1 - x_i^2}, & i = j \neq 1, N - 1 \\ \frac{2N^2 + 1}{6}, & i = j = 0 \\ -\frac{2N^2 + 1}{6}, & i = j = N \end{cases} \quad (2.17)$$

As a discretization of the PDE system, the continuum variables correlating to the time delay are discretized along the grid of  $N$  points. It is notable that the last  $n$  rows illustrate the boundary condition which defines the matrices being introduced into the system due to multiple time-delay signals. Since in this project only a single time delay variable is considered, only  $\mathbf{A}_1$  and state matrix  $\mathbf{A}_0$  are placed in the boundary condition row. In addition,  $N$  stands for the size of the Chebyshev differentiation matrix and therefore controlling the precision and workload of the computation. As shown in [13] the node size is not necessarily to be high in order to achieve an accurate result. The schematic of matrix  $\mathbf{M}$  with the introduction of a single time delay case is illustrated in Figure 2.1. The gray blocks are the Chebyshev discretization matrices which bear the property of sparsity. The dark blocks are the state and delayed matrix respectively, whereas the white blocks are null matrices.

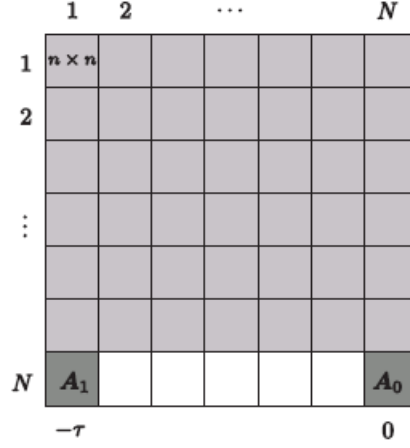


**Figure 2.1:** Matrix M structure for a system with a single time delay [1]

### 2.2.2 Padé approximants

With respect to the Padé approximation method, firstly a common time-shift property of a signal in Laplace domain shall be presented:

$$f(t - \tau)u(t - \tau) \xrightarrow{\mathcal{L}} e^{-\tau s} F(s) \quad (2.18)$$

where  $s$  is the Laplace domain variable,  $u(t - \tau)$  is the step response with time delay  $\tau$  and  $F(s)$  is the Laplace transformation of  $f(t)$ . One can observe that an exponential term has been introduced in Laplace domain when signals are delayed. Moreover, if this exponential term is expanded through Taylor's expansion to obtain a rational polynomial fraction, an approximated time-domain function could be derived from the inverse Laplace transform of the polynomial function. As we can see from the equations shown below, where the final approximation function  $\phi(t)$  is derived:

$$\begin{aligned} e^{-\tau s} &= 1 - \tau s + \frac{(\tau s)^2}{2!} - \frac{(\tau s)^3}{3!} + \dots \\ &\approx \frac{b_0 + b_1 \tau s + \dots + b_q (\tau s)^q}{a_0 + a_1 \tau s + \dots + a_p (\tau s)^p} \end{aligned} \quad (2.19)$$

$$e^{-\tau s} F(s) \approx P(s) F(s) \xrightarrow{\mathcal{L}^{-1}} \phi(t) \quad (2.20)$$

It is worthy to mention that the coefficients  $a_1$  to  $a_p$  and  $b_1$  to  $b_q$  are calculated through the division of the right-side polynomials and equating them to the first  $p+q$  counterparts



in Taylor's expansions function. Here  $s$  is the continuous Laplace domain variable, whereas in the Chebyshev discretization scheme, the variable  $\lambda$  is discrete.

Normally  $p$  and  $q$  are chosen to be 6 due to the limitation imposed from the binary floating point precision as explained in [1]. From this condition, the denominators and numerators' coefficients could be computed through the following criterion:

$$\begin{aligned} a_o &= 1 \\ a_i &= a_{i-1} \frac{p-i+1}{i \cdot (2p-i+1)} \\ b_i &= (-1)^i \cdot a_i \end{aligned} \tag{2.21}$$

It is noticeable that Padé approximants do not deal with the characteristic matrix derived before, but rather change the original DDAE problem to a set of DAEs where time-delay variables are approximated through multiple state variables, as shown in equations (2.22) to (2.24) with the expansion of an example variable  $u$ .

$$u_d = \tilde{x}_1 + b_1 \tau \tilde{x}_2 + \dots + b_{p-1} \tau^{p-1} \tilde{x}_p + b_p \tau^p \dot{\tilde{x}}_p \tag{2.22}$$

$$\dot{\tilde{x}}_i = \tilde{x}_{i+1}, i = 1, 2, \dots, p-1 \tag{2.23}$$

$$a_p \tau^p \dot{\tilde{x}}_p = u - (a_0 \tilde{x}_1 + a_1 \tau \tilde{x}_2 + \dots + a_{p-1} \tau^{p-1} \tilde{x}_p) \tag{2.24}$$

In (2.23) we can see that each of the states being introduced into the approximation is the differential of the previous states, and variable  $u$  is introduced with  $p$  states from  $\tilde{x}_1$  to  $\tilde{x}_p$ , with the last component  $\dot{\tilde{x}}_p$  subsequently computed through the equation (2.24). Apparently there are no constraints on the number of time delays that can be introduced into the system, nor a structural divergence between multiple and single time delay cases.

Overall, both methods are approaches to approximate the full spectrum of the DDAE model. Later, two methods would be implemented into the DDAE model derived from the existing Voltage Source Converter (VSC) control scheme. Furthermore, both eigenvalue spectrums would be compared with the same conditions applied.

## Chapter 3

# System Modelling

In this chapter a full VSC controller architecture is indicated with the inclusion of various measurement time-delay signals. Meanwhile, a proposed DDAE model characterizing the small-signal stability of the existing VSC control scheme at different state is displayed.

### 3.1 VSC control scheme

The original VSC control scheme is presented in Figure 3.1. The output of the converter is connected to either a Single Machine Infinite Bus (SMIB) grid or simply an active power load through a Low-Pass Filter (LPF) and a transformer. Inside the controller there are two functioning fields which are differentiated mainly by the inner or outer control loop. Within the inner control loop there are SRF Voltage Controller and SRF

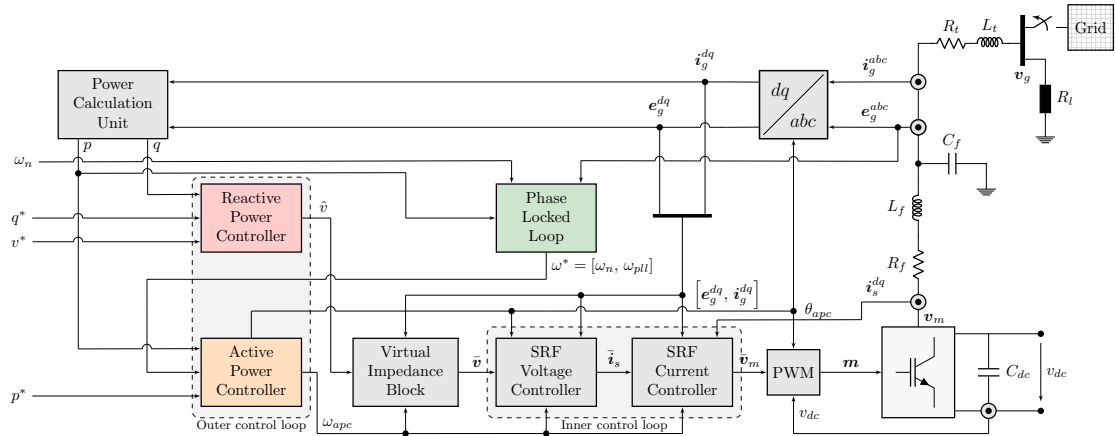


**Figure 3.1:** Original VSC control scheme. [2]

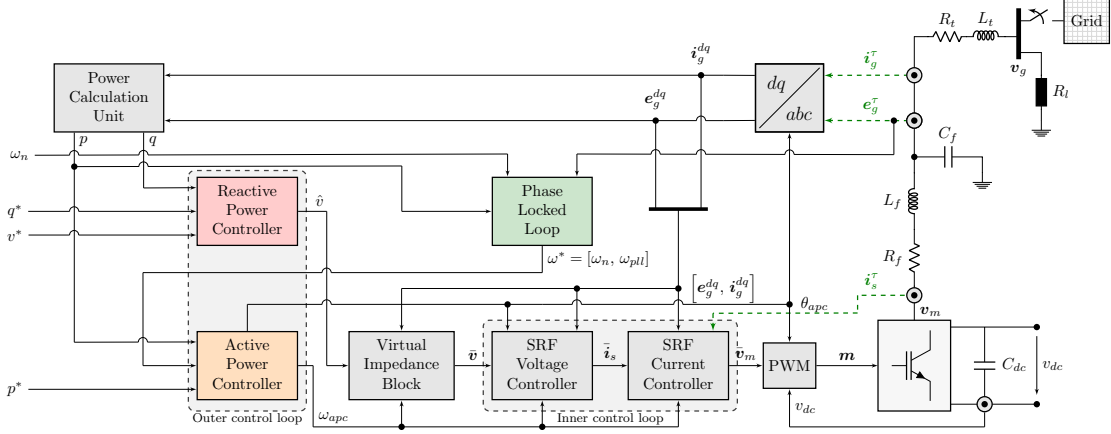


**Figure 3.2:** Same time on three measurement signals.

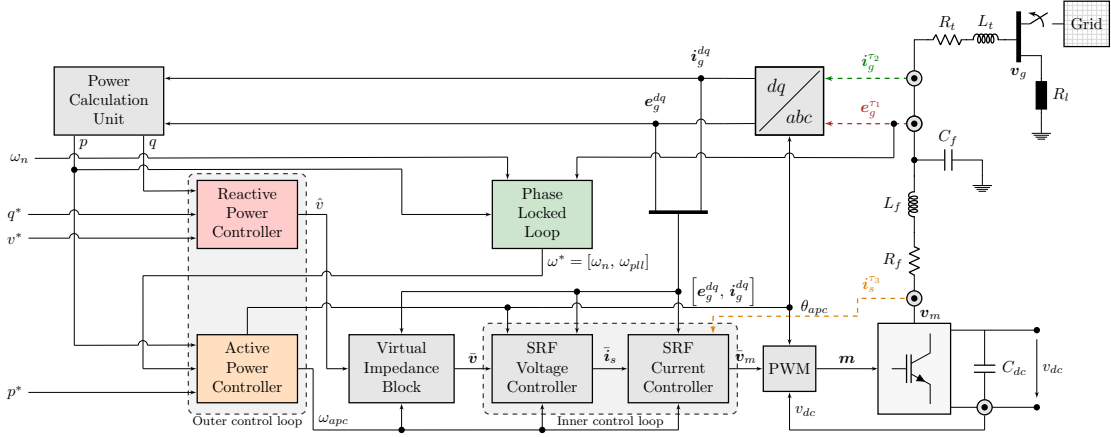


**Figure 3.3:** Various time on three measurement signals.

Current Controller, which are mainly used to prevent voltage and current saturation [8]. The outer control loop comprises of Active Power Controller (APC) and Reactive Power Controller (RPC) for tracking both frequency and voltage of the electrical system conditions. Within the APC there are two modes: Virtual Inertia Emulation controller and Droop-based controller. The Phase Locked Loop (PLL), which is used to synchronize a grid-following converter to the grid. Further discussion regarding these modes will be illustrated in the following chapter.

In this project, firstly three same time-delay measurement signals are introduced into the VSC system. As shown in Figure 3.2, voltage and current from the primary side of the grid and the output current from the converter ( $e_g^\tau$ ,  $i_g^\tau$ ,  $i_s^\tau$ ) are denoted with green colour. Subsequently a multiple time delay case is introduced with  $e_g^\tau$ ,  $i_g^\tau$  and  $i_s^\tau$  denoted in different colours, as shown in Figure 3.3. Further analysis will be focused on the impact of critical time delay from various measurements signal and identifying the most

sensitive states.

## 3.2 DDAE model

The DDAE model consists of Differential equations  $\mathbf{f}$  and Algebraic equations  $\mathbf{g}$ . In [2] a full DAE model has been established. Based on the existing DAE model, a DDAE model will be depicted briefly in the following equations, which will also be categorized into the specific sections depending on their functionality. Further details regarding the DAE model can be referred in [2].

### 3.2.1 Electrical system modeling

As mentioned in the last chapter that only measurement signals are introduced with time delays. Hence, the electrical states of the grid are computed without time-delay variables in three differential equations:

$$\dot{\mathbf{i}}_s = \frac{\omega_b}{l_f}(\mathbf{v}_m - \mathbf{e}_g) - \left( \frac{r_f}{l_f} \omega_b + j\omega_b \omega_g \right) \mathbf{i}_s \quad (3.1)$$

$$\dot{\mathbf{i}}_g = \frac{\omega_b}{l_g + l_t}(\mathbf{e}_g - \mathbf{v}_g) - \left( \frac{r_g + r_t}{l_g + l_t} \omega_b + j\omega_b \omega_g \right) \mathbf{i}_g \quad (3.2)$$

$$\dot{\mathbf{e}}_g = \frac{\omega_b}{c_f}(\mathbf{i}_s - \mathbf{i}_g) - j\omega_g \omega_b \mathbf{e}_g \quad (3.3)$$

where  $\mathbf{i}_s$  is the switching current at the output of the converter,  $\mathbf{i}_g$  and  $\mathbf{e}_g$  are the current and voltage at the primary side of the transformer connecting to the grid respectively,  $\mathbf{v}_m$  indicates the modulation voltage and  $\mathbf{v}_g$  represents the grid voltage. Meanwhile, the active and reactive power output of the converter are fed into the VSC controller. Consequently, time-delay variables, which are denoted in different colours, are introduced to the power calculation block as shown in the following algebraic equations:

$$p = e_{g\tau}^d i_{g\tau}^d + e_{g\tau}^q i_{g\tau}^q \quad (3.4)$$

$$q = e_{g\tau}^q i_{g\tau}^d - e_{g\tau}^d i_{g\tau}^q \quad (3.5)$$

### 3.2.2 Phase-Locked Loop

This synchronization unit detects and estimates the grid frequency and further maintains synchronization of VSC controller to the grid in the grid-following mode. Mathematical expression of differential and algebraic equations in PLL are presented here:

$$\dot{\varepsilon} = \hat{e}_g^q \quad (3.6)$$

$$\dot{\vartheta}_{pll} = \nu_{pll} \omega_b \quad (3.7)$$

$$\nu_{pll} = \omega_n - \omega_g + K_p^{pll} \hat{e}_g^q + K_i^{pll} \varepsilon \quad (3.8)$$

where  $\vartheta_{pll}$  and  $\nu_{pll}$  are estimated frequency and angle, while  $\omega_n$  and  $\varepsilon$  are nominal frequency and integrator state.

It is noticeable that in the grid-forming mode the frequency set-point signal is passed through the PLL directly to the APC block. Hence the above equations are simplified as a single equation:

$$\nu_{pll} = \omega_n \quad (3.9)$$

### 3.2.3 Active Power Control

For Active Power Droop Control (APDC) two differential equations and one algebraic equation are illustrated as follows:

$$\dot{\vartheta}_{apc} = \nu_{apc}\omega_b \quad (3.10)$$

$$\dot{\tilde{p}} = \omega_c(p - \tilde{p}) \quad (3.11)$$

$$\nu_{apc} = \nu_{pll} + D_p(p^* - \tilde{p}) \quad (3.12)$$

where  $\vartheta_{apc}$  denotes the phase angle of APC,  $\nu_{apc}$  is the output frequency of APC after SRF alignment and  $\tilde{p}$  stands for filtered-power-measurement signal. A droop gain  $D_p$  is adopted to adjust the output frequency depending on the discrepancy between the measured power and the power set-point signal  $p^*$

In the case of Virtual Inertia Emulation (VIE) mode, equations (3.11) and (3.12) are replaced with following equations:

$$\dot{\omega}_{apc} = \frac{1}{2H}(p^* - p) - \frac{1}{2H}K_d(\omega_{apc} - \omega^*) \quad (3.13)$$

$$\nu_{apc} = \omega_{apc} + \omega_g \quad (3.14)$$

This mode emulates the synchronous machine swing equation expression, where electrical power and mechanical power are substituted by set-point power  $p^*$  and output active power as in equation (3.13).

### 3.2.4 Other DDAEs

For the sake of simplicity and without loss of generality, the remaining DDAEs are placed together, since these equations are identical for different cases being applied to the VSC controller.

The differential equations for reactive power controller, SRF voltage and current controllers are listed in the following equations respectively:

$$\dot{\tilde{q}} = \omega_c(q - \tilde{q}) \quad (3.15)$$

$$\dot{\tilde{\xi}} = \bar{v} - \mathbf{e}_{g\tau} \quad (3.16)$$

$$\dot{\tilde{\gamma}} = \bar{\mathbf{i}}_s - \mathbf{i}_{s\tau} \quad (3.17)$$

with  $\tilde{q}$ ,  $\xi$  and  $\gamma$  representing LPF value of reactive power, integrator state of SRF voltage and current controller, respectively.

For algebraic equations derived from the other controller models:

$$\hat{v} = v^* + D_q(q^* - \tilde{q}) \quad (3.18)$$

$$\bar{v}^d = \hat{v} - r_v \dot{i}_{g\tau}^d + \omega_{apc} l_v \dot{i}_{g\tau}^q \quad (3.19)$$

$$\bar{v}^q = -r_v \dot{i}_{g\tau}^q + \omega_{apc} l_v \dot{i}_{g\tau}^d \quad (3.20)$$

$$\bar{i}_s = K_p^v(\bar{v} - e_{g\tau}) + K_i^v \xi + j\omega_{apc} c_f e_{g\tau} + K_f^i \dot{i}_{g\tau} \quad (3.21)$$

$$\bar{v}_m = K_p^i(\bar{i}_s - \dot{i}_{s\tau}) + K_i^i \gamma + j\omega_{apc} l_f \dot{i}_{s\tau} + K_f^v e_{g\tau} \quad (3.22)$$

$$v_m = \bar{v}_m \quad (3.23)$$

Now with different settings of DDAE model being established, we can further compare the numerical results between Chebyshev discretization method and Padé Approximation technique.

## Chapter 4

# Eigenvalue Spectrum Analysis

A crucial criterion that the real part of rightmost eigenvalue equals to zero corresponding to the boundary condition between stable and unstable zones was established to judge the stability of the system based on the eigenvalue spectrum. This offers an efficient method to distinguish between the stable and unstable system when time delays are stepped up discretely. With this conclusion, several findings of this project will be explained in the following sections.

### 4.1 Very small time-delay: DDAE vs. DAE

As we can see from Figure 4.1, a very small time-delay of  $\tau=1 \mu s$  has been applied to the DDAE system using both Chebyshev discretization and Padé Approximants and is compared with the original DAE model where time-delay signals are not included. The three eigenvalue spectrums overlap with each other and share almost the same value at each position of the roots. This result has confirmed that both approximation techniques are applicable and feasible to properly approximate the eigenvalue spectrum.

Moreover, the rightmost eigenvalue still lies left of the imaginary axis, indicating that the system is stable when no or low time delay is introduced. As can be seen further in the next section, when the time delay is stepped up discretely, the eigenvalue spectrum experiences a shifting trend until it passes stable boundary.



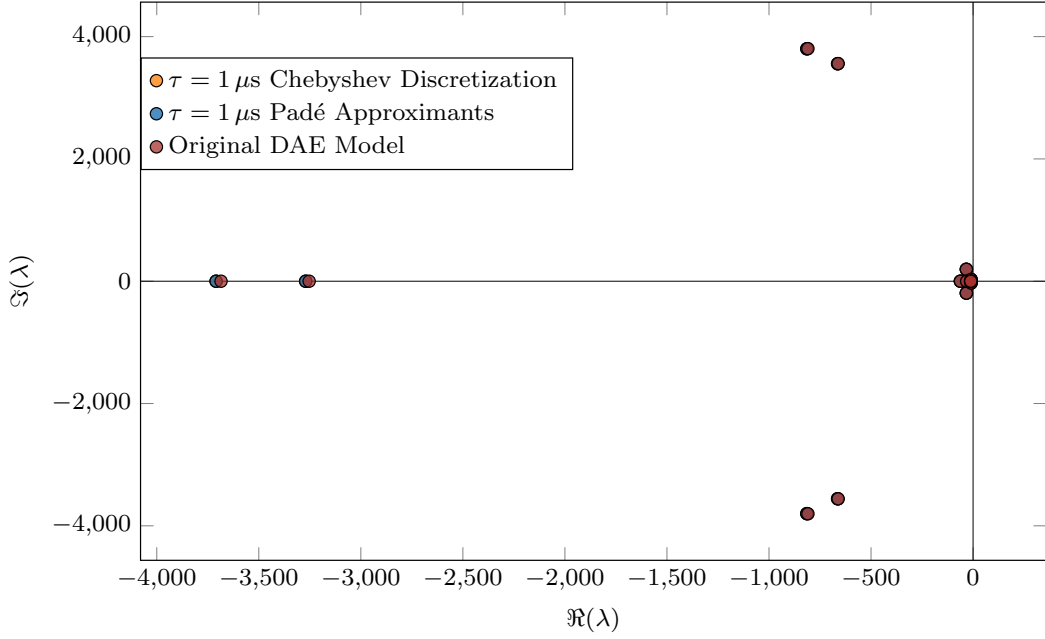


**Figure 4.1:** Eigenvalues of DAE and DDAE using Chebyshev and Padé Approximation

## 4.2 Same time delay for all measurement signals

In this section, a discrete step increase of measurement time delays are applied from  $50 \mu s$  to  $300 \mu s$ . Figure 4.2 and Figure 4.3 display full eigenvalue spectrum achieved from Padé approximation and Chebyshev discretization respectively. However, we can hardly see any consistency between these two spectrums in terms of the position range of the roots. This is due to the fact that the essence of these two methods is different. Chebyshev discretization technique transforms the original characteristic matrix to a PDE system and then implemented the finite element method to discretize the matrix. Subsequently, the derived matrix is expanded and, hence, resulting in the inclusion of redundant roots along with the original solutions. While for Padé approximation only the retarded state variables have been implemented with Taylor's Expansion. Therefore, the size of the original characteristic matrix is kept intact and unchanged. Consequently, the eigenvalues computed through this method will produce the same amount of eigenvalues as in the subset of the original spectrum. Nevertheless, a shift of eigenvalues to the right half spectrum could be witnessed for both cases. Since the criteria for determining the stability of the system lies at the rightmost eigenvalues. A further reduced range of spectrum would be considered in the following, as can be seen from Figure 4.4 and 4.5.

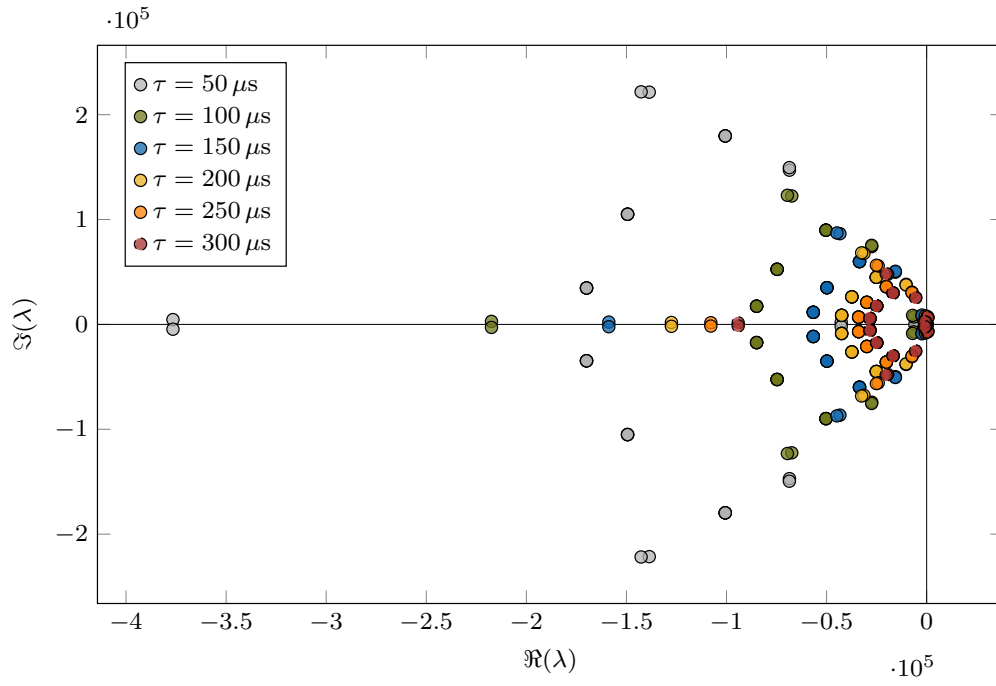


**Figure 4.2:** Full eigenvalue spectrum computed using Padé approximation for time delay

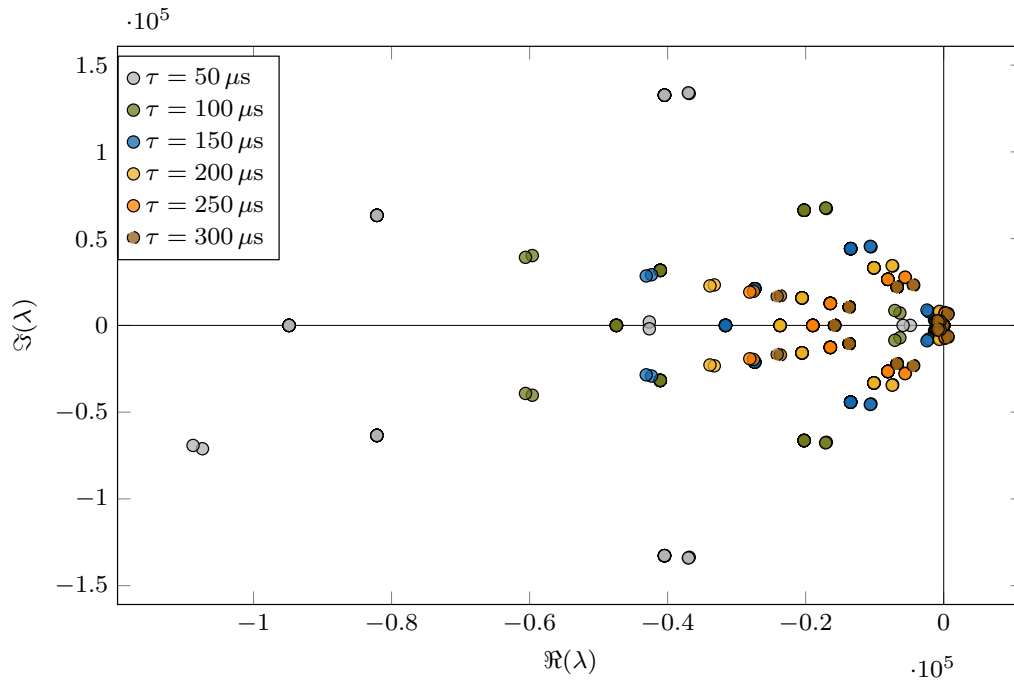


**Figure 4.3:** Full eigenvalue spectrum computed using Chebyshev discretization for time delay

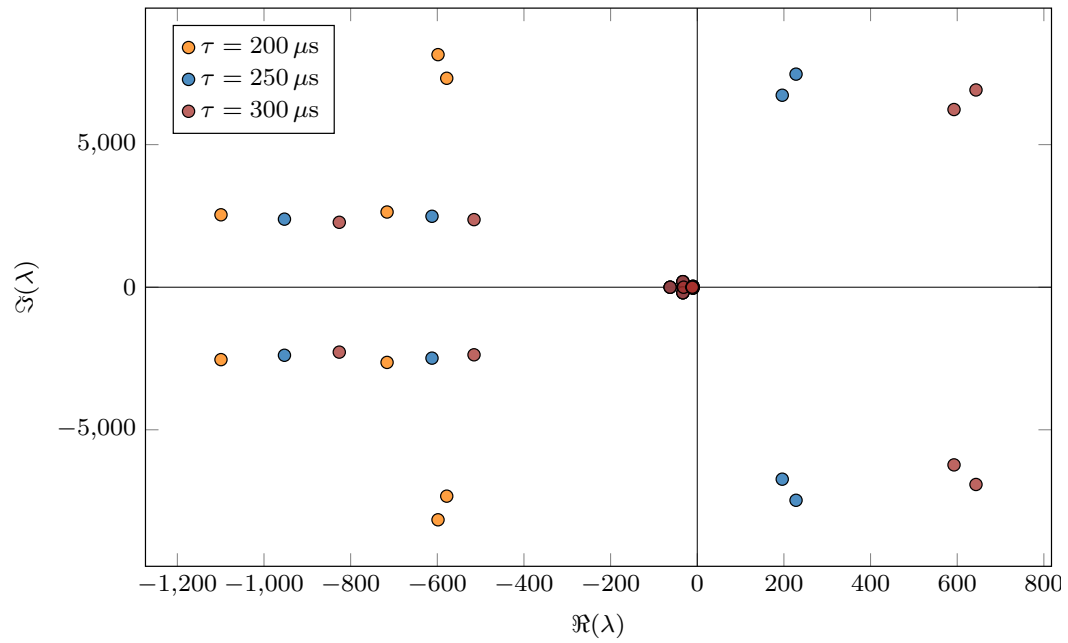


**Figure 4.4:** Critical eigenvalues computed using Padé approximation for time delay

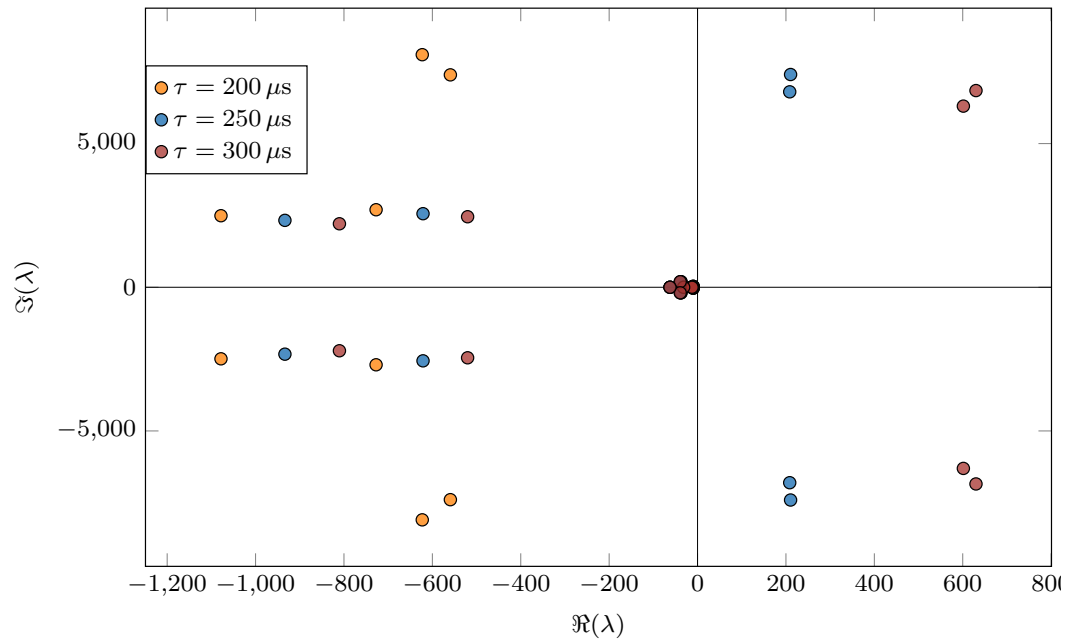


**Figure 4.5:** Critical eigenvalues computed using Chebyshev discretization for time delay

The discrete step ranges from 200 to 300  $\mu s$  for both techniques. Both methods offer

almost the same results for the reduced eigenvalue spectrum regarding position and movement trend. The whole eigenvalue spectrum is continuously shifting to the right until the first two eigenvalues, which are conjugates of each other, first arrive at the imaginary boundary, forming the critical stability condition of the whole system. In addition, the critical time delay computed from both techniques yields the same result,  $233 \mu s$ . This critical time delay has also been verified through non-linear Electromagnetic Transient simulations in Simulink on a detailed non-linear converter model. For the sake of simplicity, only Padé approximants results would be provided in the following sections of the report.

### 4.3 Eigenvalue Analysis for Single Time Delay

From the last section, when same measurement time delays have been applied to the system, one can observe the critical time delay lies at  $233 \mu s$ . Accordingly, a further analysis regarding each of the measurement signal has to be conducted to identify which measurement signal is the most critical one. Hence, three single time delay cases are demonstrated below. We will begin with the results obtained from  $e_g^\tau$  introduced case.

#### 4.3.1 Single time delay: $e_g^\tau$

As can be seen from Figure 4.6, only voltage measurement has been introduced with time delays, whereas the other two measurement signals do not involve any time delays.  $e_g^\tau$  is increased in discrete steps of  $150 \mu s$  in a full eigenvalue spectrum as shown in Figure 4.7, followed by a reduced eigenvalue spectrum in Figure 4.8.

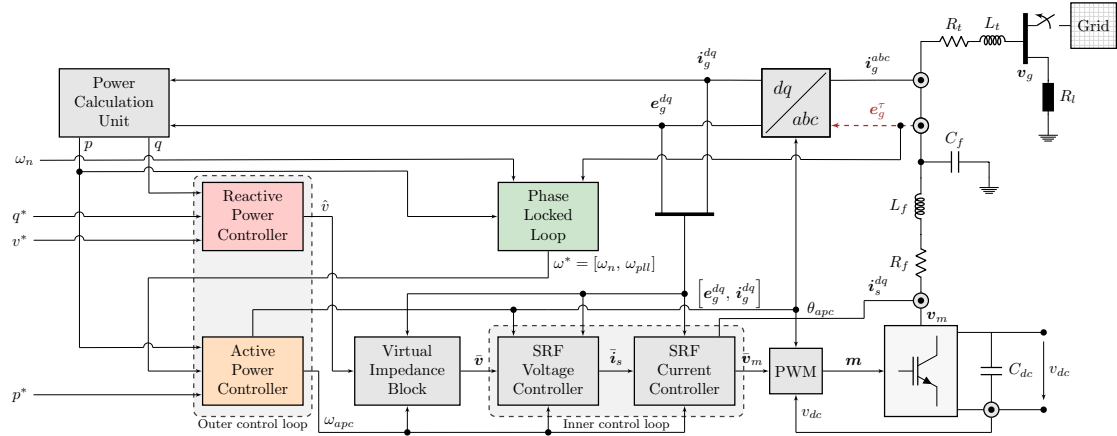
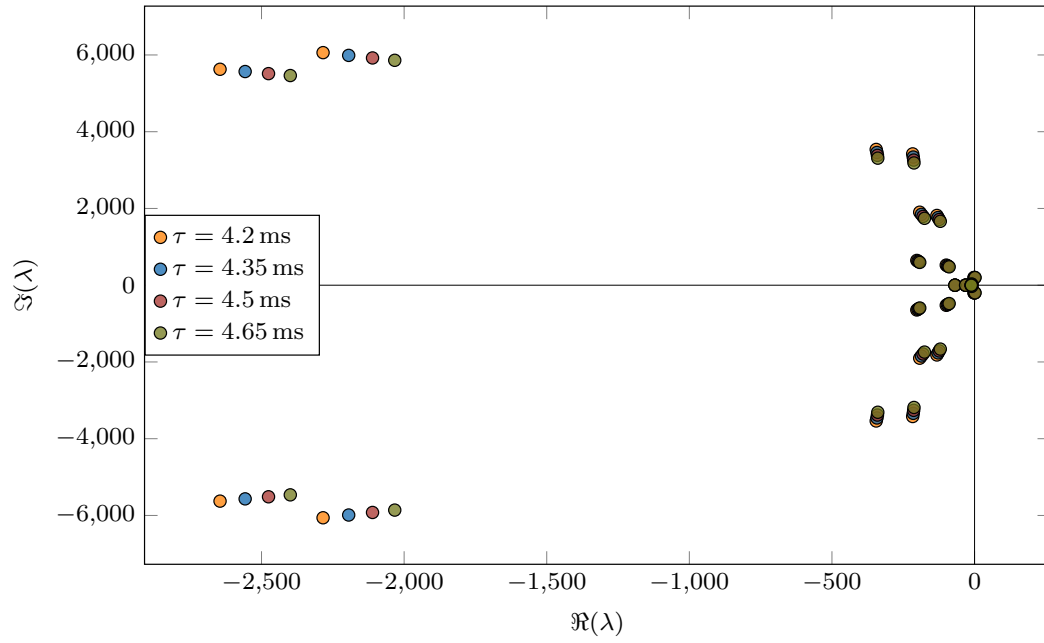
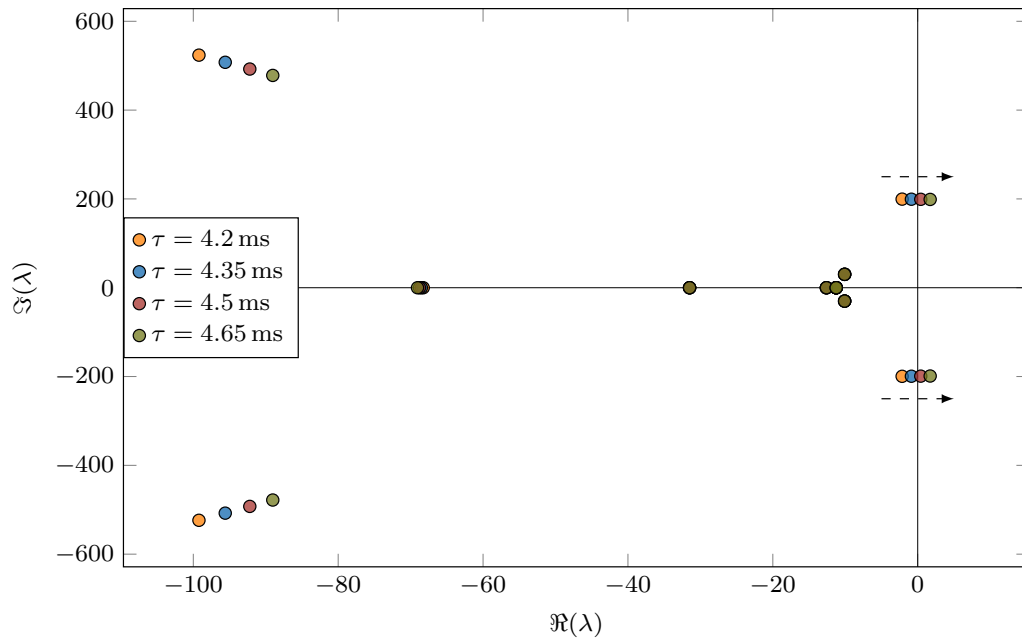


Figure 4.6:  $e_g^\tau$  introduced in VSC control structure



**Figure 4.7:** Single time delay introduced by  $e_g^\tau$  ranging from 4200 to 4650  $\mu\text{s}$



**Figure 4.8:** Single time delay introduced by  $e_g^\tau$  ranging from 4200 to 4650  $\mu\text{s}$  in a reduced range

As can be seen from the full eigenvalue spectrum of the single  $e_g$  time delay case, the rightmost eigenvalue shifts towards right-half plane when time delay has been increased up to 4.5 ms. The critical time delay for the VSC system is 4.451 ms exactly. This time delay is an order of magnitude larger than the critical time delay of 233  $\mu$ s presented earlier. Hence, further research on the other measurement signals is necessary.

### 4.3.2 Single time delay: $i_g^\tau$

In this section only the measurement current of the grid is introduced with time delay, symbolizing with  $i_g^\tau$  in the VSC controller scheme as shown in Figure 4.9. The current time delay  $i_g^\tau$  is increased in discrete steps of 100  $\mu$ s.

Same pattern could be observed for grid current measurement delay case as in the grid voltage case. The critical delay time for  $i_g^\tau$  is 1.573 ms specifically, significantly higher than the 233  $\mu$ s achieved in the same measurement time-delay case. Hence, both  $e_g$  and  $i_g$  should not be critical states responsible for the stability margin of the system.

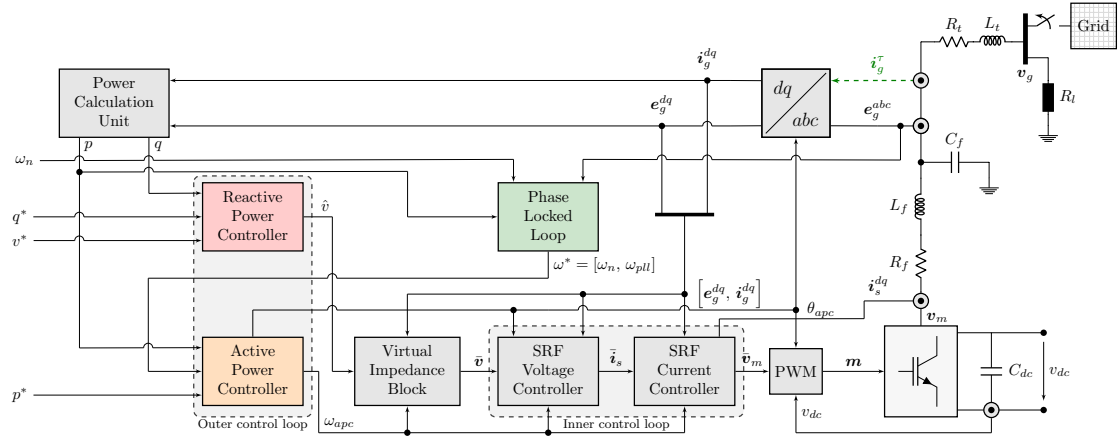
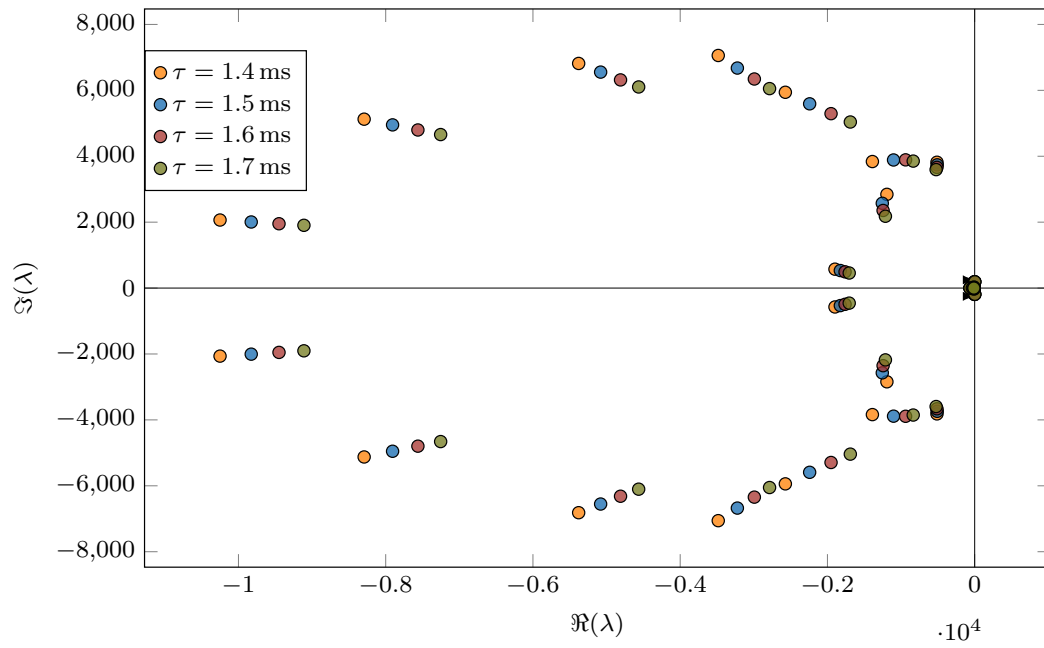
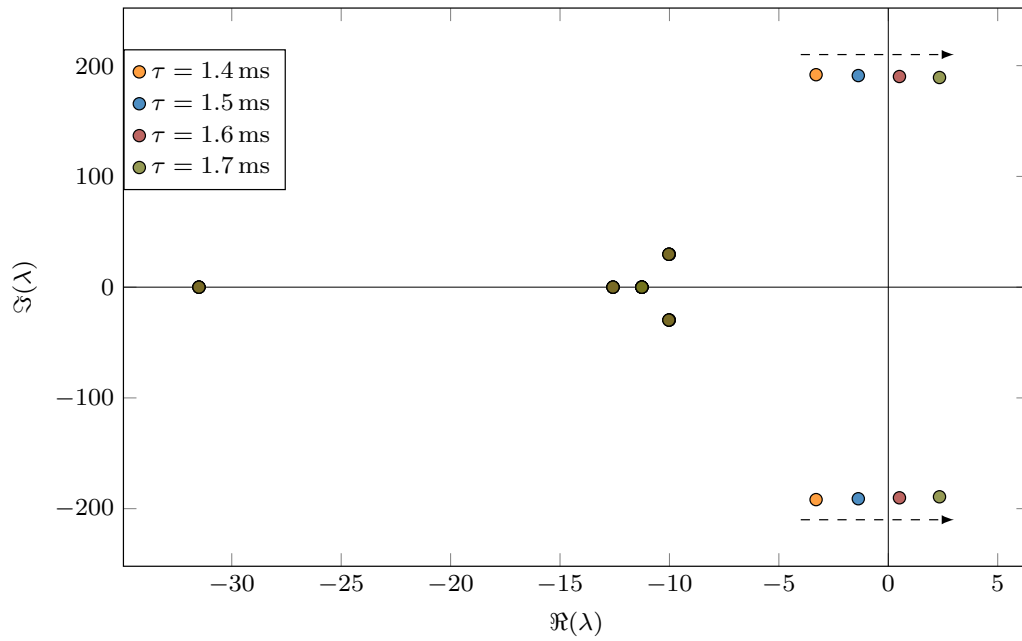


Figure 4.9:  $i_g^\tau$  introduced in VSC control structure



**Figure 4.10:** Single time delay introduced by  $i_g^\tau$  ranging from 1400 to 1700  $\mu$ s



**Figure 4.11:** Single time delay introduced by  $i_g^\tau$  ranging from 1400 to 1700  $\mu$ s in a reduced range

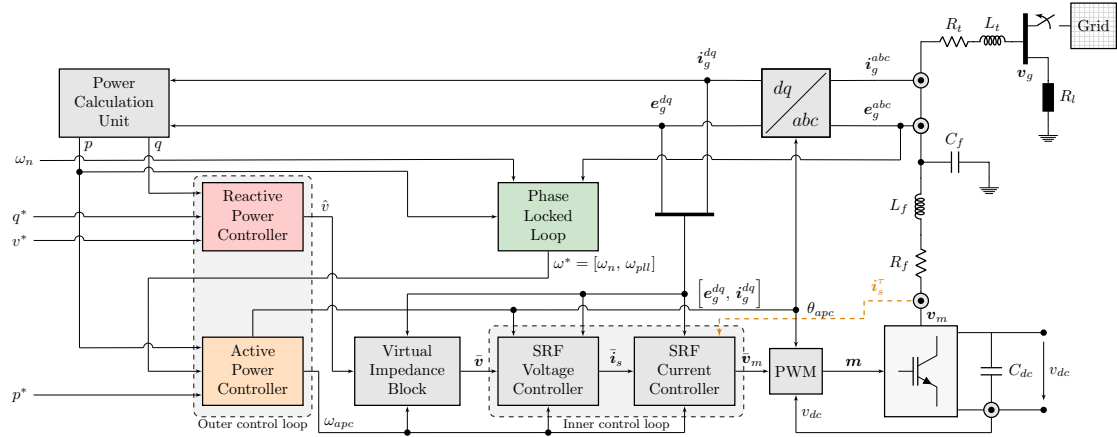


Figure 4.12:  $i_s^\tau$  introduced in VSC control structure

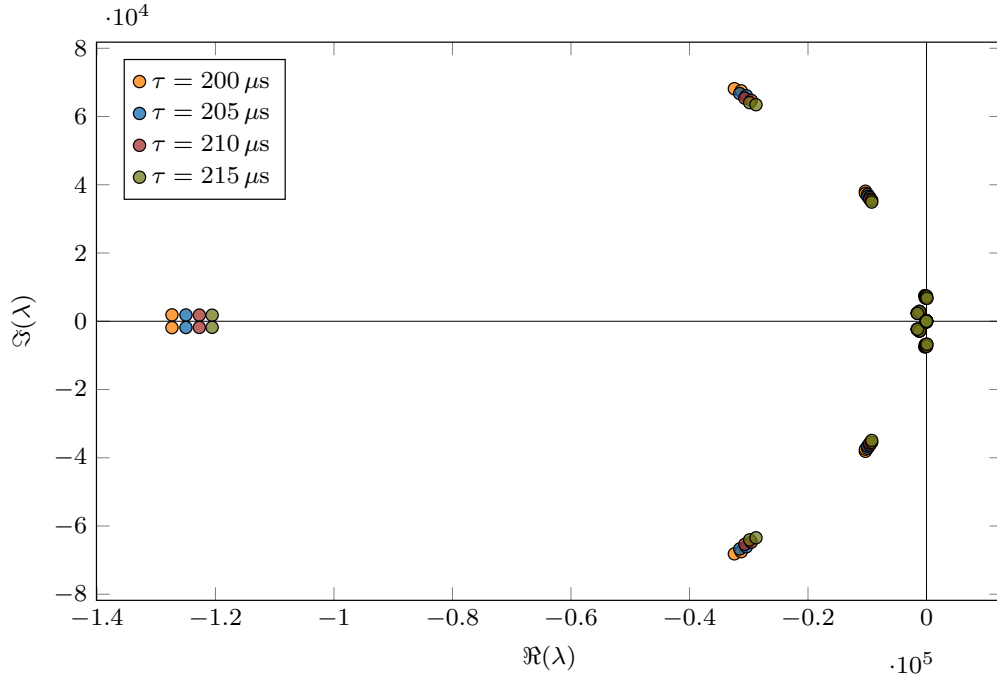
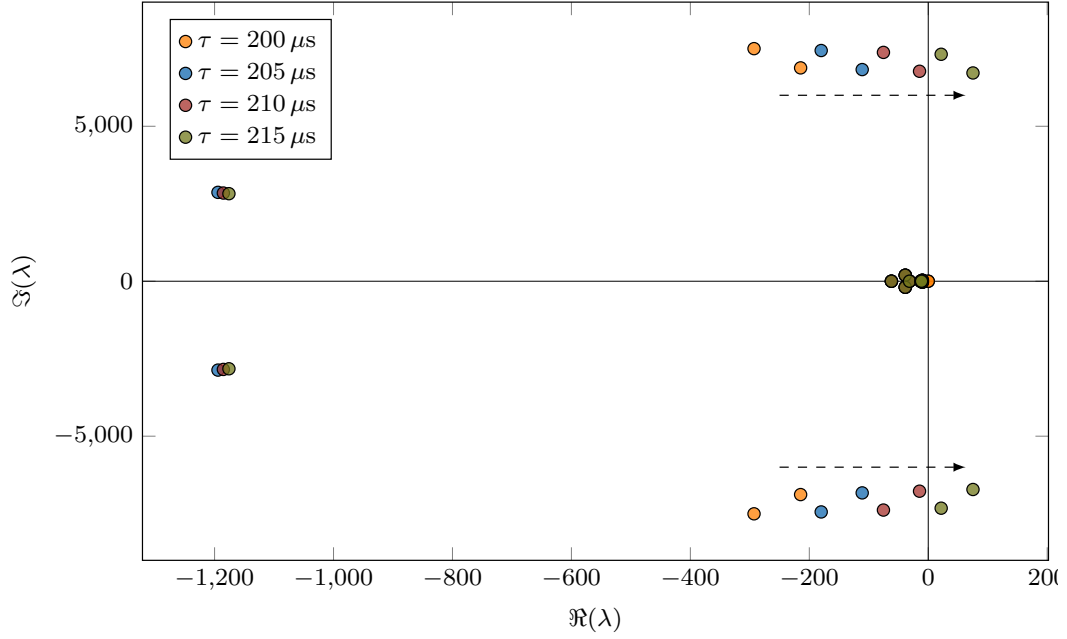


Figure 4.13: Single time delay introduced by  $i_s^\tau$  ranging from 200 to 215  $\mu s$

### 4.3.3 Single time delay: $i_s^\tau$

In this case, time delay is introduced only to the converter output current measurement, as can be seen from Figure 4.12. The current time delay  $i_s^\tau$  is increased in discrete steps of 5  $\mu s$ .





**Figure 4.14:** Single time delay introduced by  $i_s^\tau$  ranging from 200 to 215  $\mu s$  in a reduced range

**Table 4.1:** Critical time delay for each case

retarded variable	$e_g^\tau$	$i_g^\tau$	$i_s^\tau$
critical delay time	4.4 ms	1.6 ms	215 $\mu s$

As usual, in the reduced range of eigenvalue spectrum one can observe the shift phenomenon of the roots with the step increase of time delay. The critical time delay in this case becomes 211  $\mu s$ . This is the lowest critical time delay observed so far. Three critical measurement delays have been summarized in table 4.1.

It is clear that state  $i_g$  affects the stability margin of the system substantially comparing to the other two measurements. Besides, the single time delay of  $i_s^\tau$  is unexpectedly less than the same measurement time delay case, where 233  $\mu s$  is acquired. Henceforth, an analysis of the impact of critical time delay for  $i_s$  with respect to the changes of time delay signals  $e_g^\tau$  and  $i_g^\tau$  was carried out.

As can be seen from Figure 4.15, there is a change of critical switching current time delay when both grid voltage and current measurement signals are introduced with different time delays. From the perspective of  $\tau_{i_g}$ , the critical time delay for switching current  $\hat{\tau}_{i_s}$  is not very sensitive towards the change of  $\tau_{i_g}$ . However, the critical value of  $\hat{\tau}_{i_s}$  is affected by  $\tau_{e_g}$  dramatically. When all the measurement time delays are close to each other, the critical value for  $\hat{\tau}_{i_s}$  reaches a local maximum value. However, if the difference

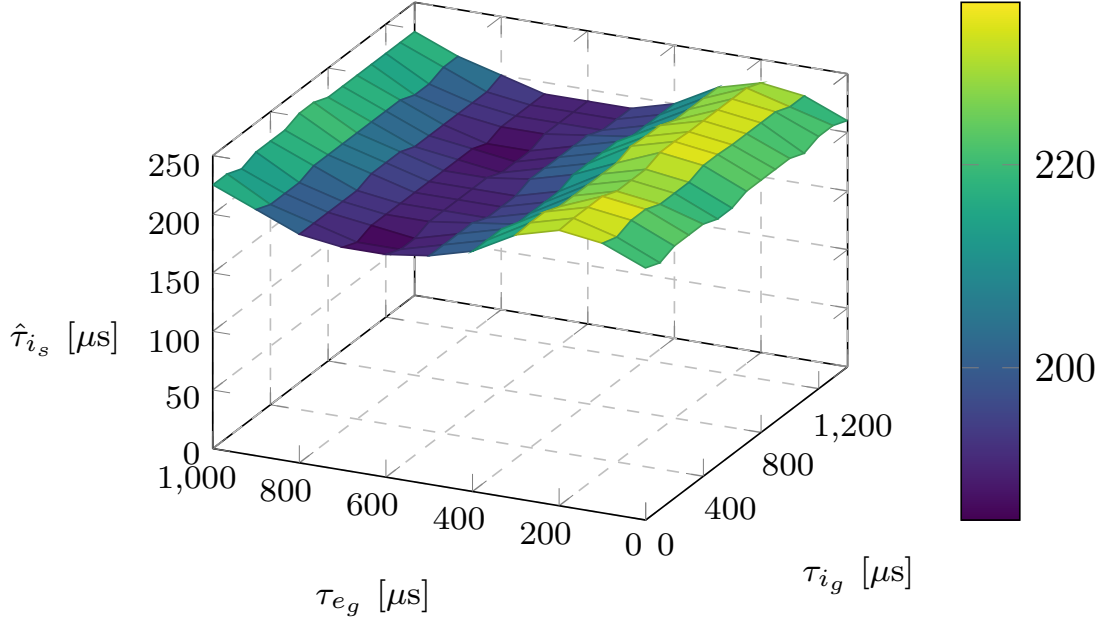


**Figure 4.15:**  $\tau_{eg}, \tau_{ig}$  affect critical time-delay  $\hat{\tau}_{i_s}$

between  $\tau_{eg}$  and  $\tau_{is}$  further increases, then  $\hat{\tau}_{i_s}$  will reduce to a lower value, resulting in a more vulnerable system. Hence, when the same measurement time delays are applied to all three signals, the critical time delay  $233 \mu s$  will be higher than single time delay being introduced to  $i_g^\tau$  only.

Further observation could be made that both measurement signals  $e_g^\tau, i_g^\tau$  are fed into all of the control units in the VSC system, while  $i_s^\tau$  is only used as the input signal for the inner control loop. This will lead to a hypothesis that the inner loop is the most vulnerable control unit to the measurement delays. Accordingly, a further simulation for both virtual inertia emulation and droop-based APC grid-forming case are used to verify the assumptions made for the inner control loop.

Figure 4.16 shows the eigenvalue spectrum for the same time delay being applied to three measurement signals, while employed with VIE controlled APC in the grid-following mode. Figure 4.17 displays the results for the grid-forming setting of the VSC system. These two plots verify the aforementioned inner loop hypothesis, as the critical time delay of  $233 \mu s$  for both configurations remains the same. Thus, further analysis of the inner control loop would be conducted to assess the critical parameters of the controller with respect to the system stability aspect.

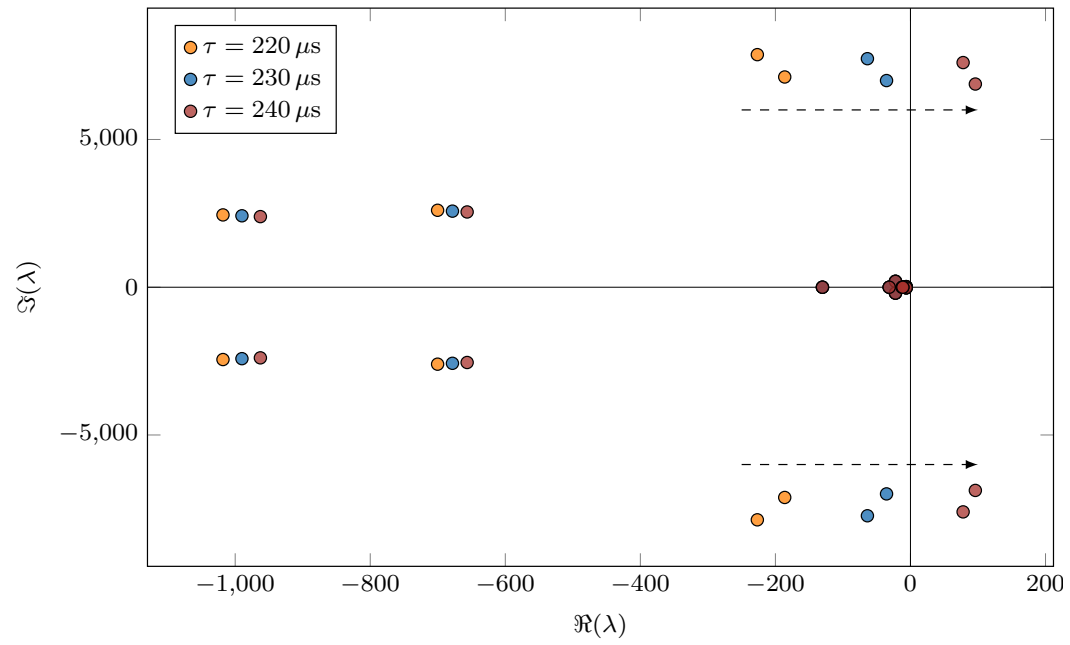


**Figure 4.16:** APC in VIE mode applying to grid-frequency following case

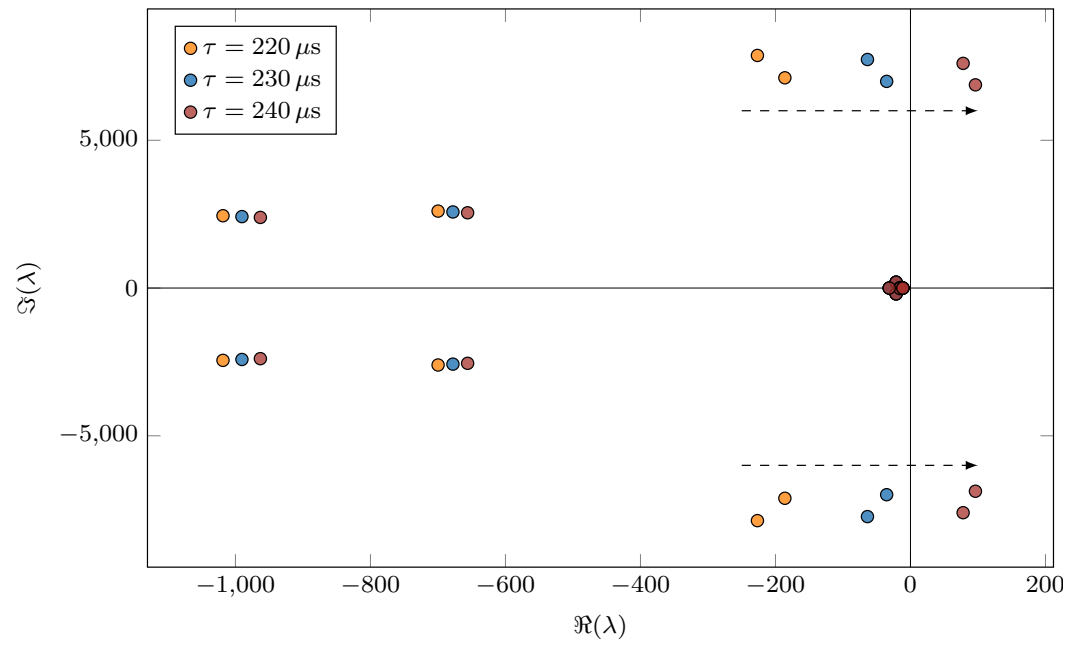


**Figure 4.17:** APC in Droop-based mode applying to grid-frequency forming case

## Chapter 5

# Stability Mapping

In the previous chapter, we observed the significant impact of the delayed switching current signal to the small-signal stability of the VSC system. Furthermore, we noticed that most vulnerable segment of the VSC controller is the inner loop. Hence, the focus of the following chapter is on proving that the current state variable contributes majorly to the stability margin of the system. Here several analysis tools have been proposed to testify this hypothesis, including participation factors and bifurcation analysis.

### 5.1 Participation factors

The contribution that each state has on a particular eigenvalue is quantified through the participation factors. In paper [15], participation factors were deployed to identify the fastest eigenvalue for Model Order Reduction process. A common formulation of the participation factors is presented in [16–18], as illustrated below:

$$p_{ki} = l_k^i r_k^i \quad (5.1)$$

where  $l_k^i$  denotes the  $k^{\text{th}}$  element of the  $i^{\text{th}}$  left eigenvector, while  $r_k^i$  represents the  $k^{\text{th}}$  element of the  $i^{\text{th}}$  right eigenvector.  $p_{ki}$  is the relative participation of the  $k^{\text{th}}$  state variable in the  $i^{\text{th}}$  mode (eigenvalue). From the definition it is clear that the higher value of participation of a state variable, the more contribution it has to the corresponding eigenvalue. The participation factors of the most critical eigenvalues are shown in Figure 5.1 and 5.2.

As can be seen from the participation factors of four critical eigenvalues  $\hat{\lambda} = 3.5697 \pm j6913.8684$  and  $\hat{\lambda} = 23.9151 \pm j7677.1995$ , the delayed switching current signal  $i_{s_\tau}$  has the highest contribution to all of the critical modes, whereas the other two measurement states  $i_{g_\tau}$  and  $e_{g_\tau}$  contribute less. It is reasonable to conclude that the SRF current

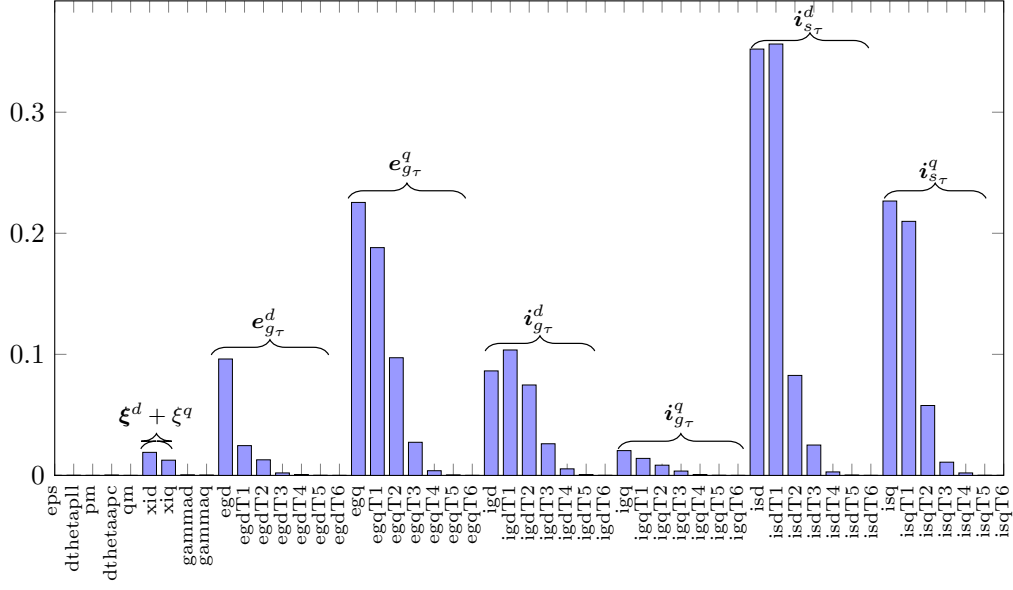


**Figure 5.1:** Participation factors for  $\hat{\lambda} = 3.5697 \pm j6913.8684$

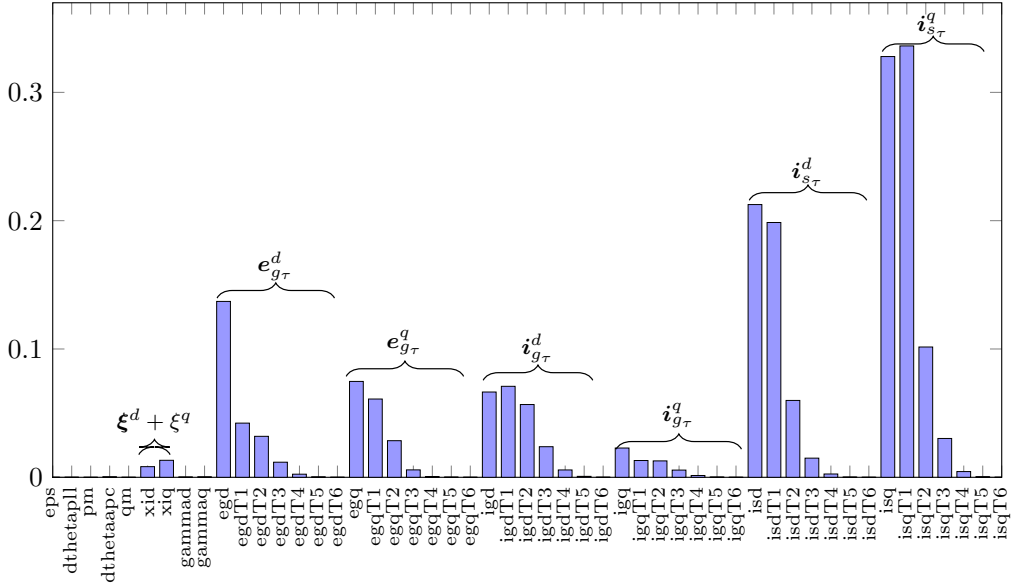


**Figure 5.2:** Participation factors for  $\hat{\lambda} = 23.9151 \pm j7677.1995$

loop is the most vulnerable controller to time delays, since it is the only controller with  $i_{s\tau}$ .

## 5.2 Bifurcation analysis

In this section same time delay case for three measurement signals is used in the bifurcation analysis. First, an SRF voltage controller parameter bifurcation test is conducted. For this test an optimized sweeping method has been implemented. Initially a rough and large discrete steps are introduced to identify the area of a dramatic critical time change. Subsequently, a more precise discretization is applied for further investigation and a two-dimensional bifurcation analysis example is showcased.

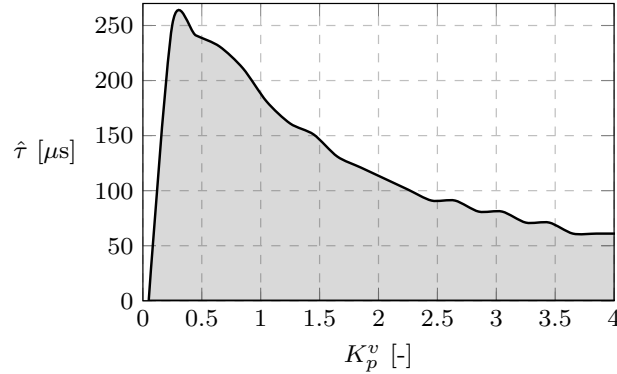
### 5.2.1 2-D bifurcation analysis

$K_p^v$  is the proportional gain of the SRF voltage controller. As can be seen from both Table 5.1 and stability map of  $K_p^v$  in Figure 5.3, there is a significant impact on the critical time delay of the system respective of the changes in the proportional gain parameter, especially when  $K_p^v$  varies from 0.5 to 1.

In terms of the integral gains of SRF voltage controller shown in Table 5.2 and Figure

**Table 5.1:** Critical time delay changes with various  $K_p^v$  ( $10\mu s$  error)

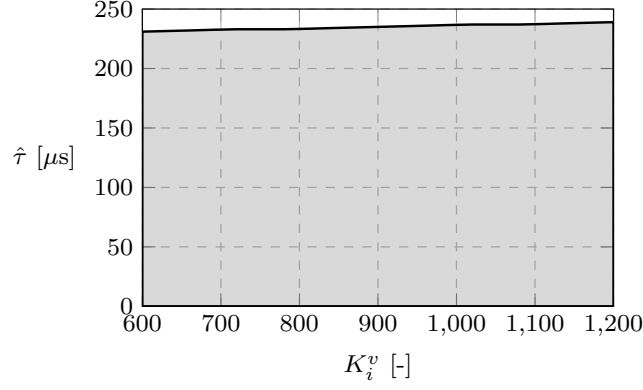
$K_p^v$	0.05	0.25	0.45	0.65	0.85	1.05	1.25	1.45	1.65	1.85	2.05
$\hat{\tau}$ ( $\mu s$ )	1.0	251	241	231	211	181	161	151	131	121	111
$K_p^v$	2.25	2.45	2.65	2.85	3.05	3.25	3.45	3.65	3.85	4.05	4.25
$\hat{\tau}$ ( $\mu s$ )	101	91	91	81	81	71	71	61	61	61	61



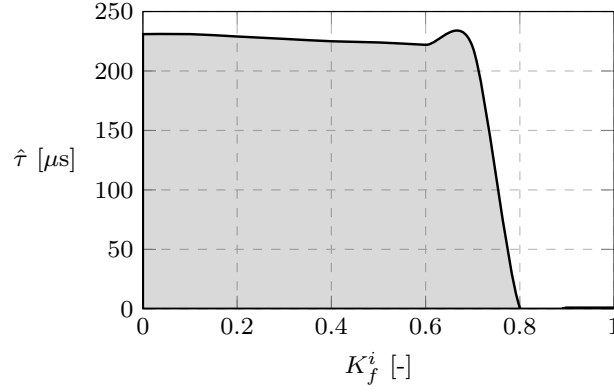
**Figure 5.3:** Stability Map on  $\hat{\tau} - K_p^v$  plane

**Table 5.2:** Critical time delay changes with various  $K_i^v$

$K_i^v$	600	660	720	780	840	900	960	1020	1080	1140	1200
$\hat{\tau}$ ( $\mu s$ )	231	232	233	233	234	235	236	237	237	238	239

**Figure 5.4:** Stability Map on  $\hat{\tau} - K_i^v$  plane**Table 5.3:** Critical time delay changes with various  $K_f^i$ 

$K_f^i$	0	0.1	0.2	0.3	0.4	0.5	0.6	0.7	0.8	0.9	1.0
$\hat{\tau}$ ( $\mu$ s)	233	231	229	227	225	224	222	220	1	1	1

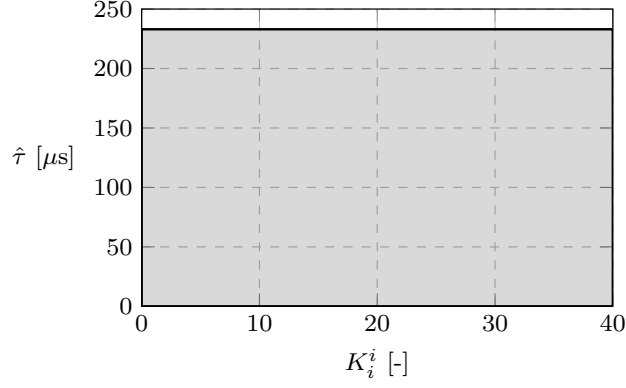
**Figure 5.5:** Stability Map on  $\hat{\tau} - K_f^i$  plane

5.4, one can observe a flat line of critical time delay as  $K_i^v$  further increases. This gives an indication that the correlation between the stability of the VSC system and the integral parameter is low.

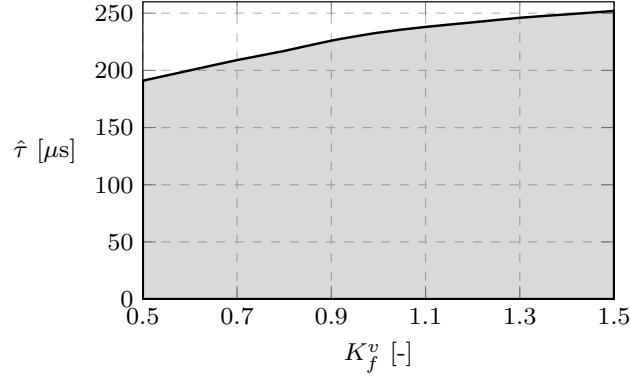
A bifurcation test upon feed-forward signal  $K_f^i$  is demonstrated in Table 5.3 and Figure 5.5. A similar pattern as in the integral gain parameter test is monitored: a flat line of critical time delay until the parameter is increased to a threshold value. Excess of this limit causes the system to collapse even without time delay being introduced into the control scheme. Hence, the correlation between the critical time delay and the feed-forward signal is also not significant.





**Figure 5.7:** Stability Map on  $\hat{\tau} - K_i^i$  plane**Table 5.6:** Critical time delay changes with various  $K_f^v$ 

$K_f^v$	0.5	0.6	0.7	0.8	0.9	1.0	1.1	1.2	1.3	1.4	1.5
$\hat{\tau} (\mu s)$	191	200	209	217	226	233	238	242	246	249	252

**Figure 5.8:** Stability Map on  $\hat{\tau} - K_f^v$  plane

ing the inner control loop details to investigate the small-signal stability of the proposed VSC system. As can be seen in Figure 5.9, the critical time delay without detailed consideration of inner loop controller is at around 250 milliseconds, drastically above what is observed in this project as microseconds. Thus, the overlook of inner control loop characteristic may cause the conclusion to be flawed. A further investigation of three-dimensional bifurcation analysis is carried out to validate our observation.

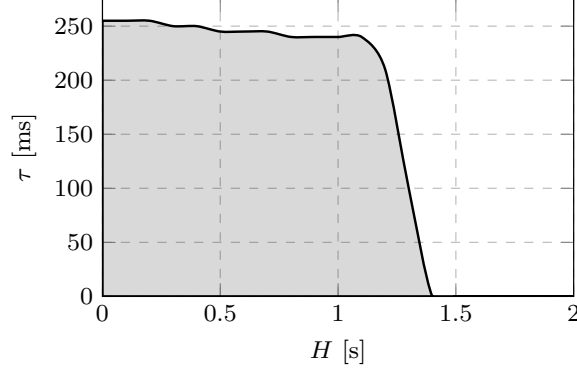


**Figure 5.9:** Stability Map on  $\hat{\tau} - H$  plane

### 5.2.2 3-D bifurcation analysis

Three-dimensional bifurcation analyzes the impact of two controller parameters on the critical time delay, forming an uneven plane to further indicates the effect of two variables simultaneously. The map in Figure 5.10 illustrates the correlation of proportional and integral gains  $K_p^v$ ,  $K_p^i$  to the critical delay time  $\hat{\tau}$ . The depicted surface indicates the stability margin of the system. Similar to what is shown in Figure 5.5, 3-D stability mapping of SRF voltage controller integral gain parameter does not influence  $\hat{\tau}$ . On the other hand, the critical time delay is sensitive towards the changes in proportional gain  $K_p^v$ . The same observation can be spotted from SRF current controller stability mapping in Figure 5.11.

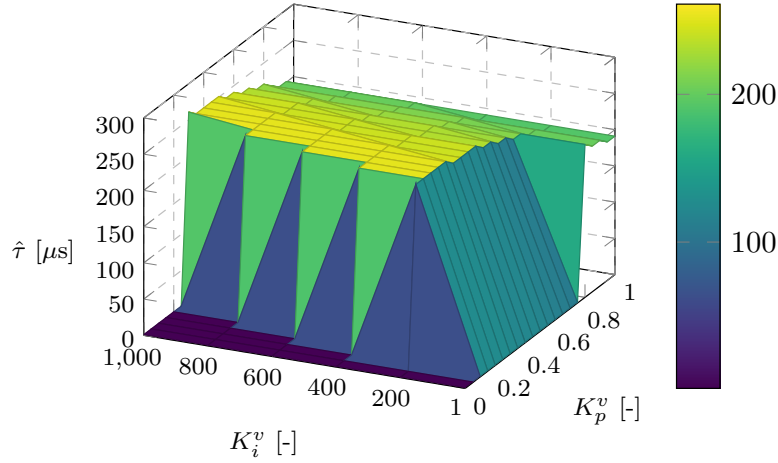


**Figure 5.10:** Stability Surface in the  $\hat{\tau} - K_p^v - K_p^i$ , System is stable under shaded area

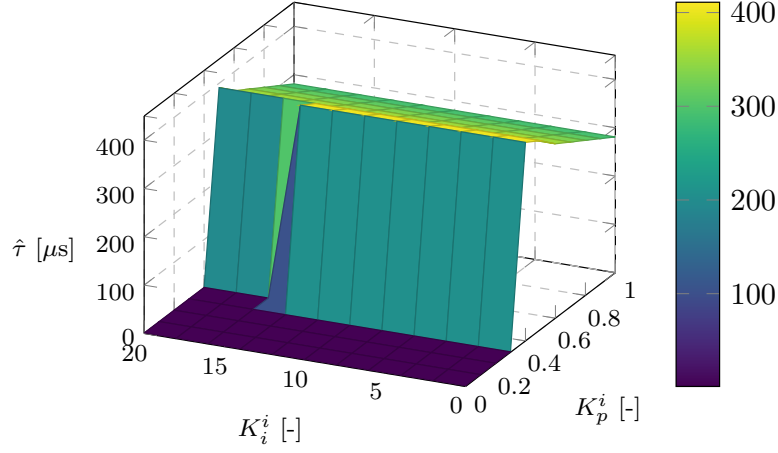


**Figure 5.11:** Stability Surface in the  $\hat{\tau} - K_p^i - K_i^i$ , System is stable under shaded area

However, a steeper cliff is showcased in the SRF current controller stability mapping than in the voltage controller. When the proportional gain varies from 0.2 to 0.4 in the current controller, a sudden plummet is observed for the critical time delay compared with a more gradual and smooth drop in the voltage controller. Therefore, we conclude that the proportional gain in the SRF current controller is more influential in the small-signal stability of the system than the voltage controller, despite both having impacts on the critical time delay.

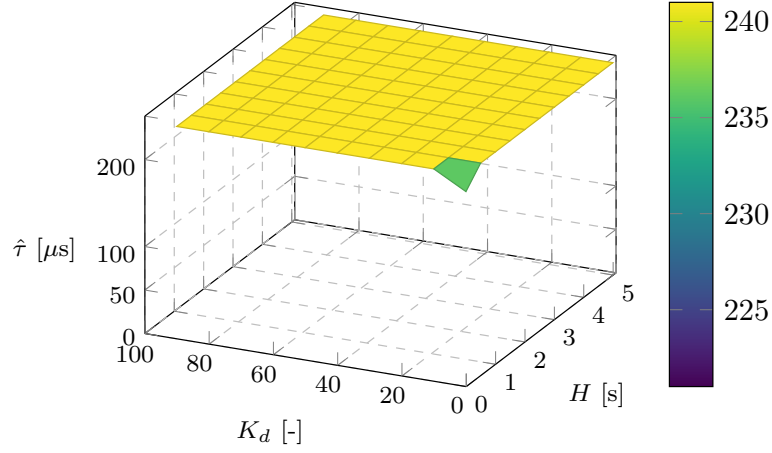


**Figure 5.12:** Stability Map on  $\hat{\tau} - K_d - H$  plane

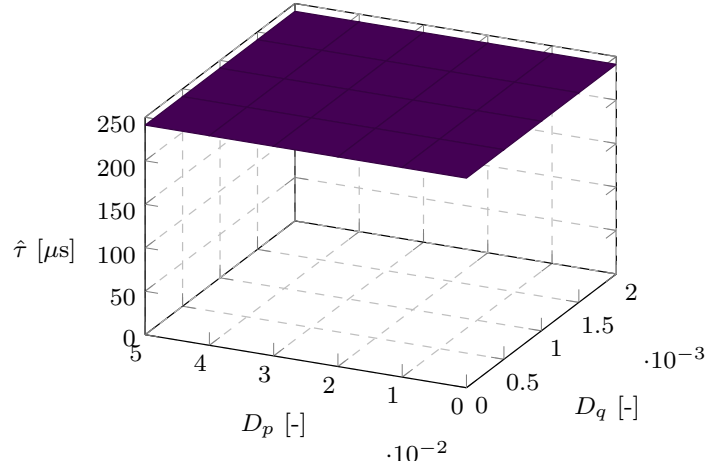


**Figure 5.13:** Stability Map on  $\hat{\tau} - D_p - D_q$  plane

With further analysis being focused on the outer control loop, we can see a somewhat different behavior, as depicted in Figure 5.12. Here, a correlation between VIE parameters (damping constant  $K_d$  and inertia constant  $H$ ) and the critical time delay  $\hat{\tau}$  is represented with a flat plane, indicating that the APC parameters essentially have no impact on the critical time delay of the system.

Meanwhile, parameter variation for active power control in Figure 5.13 and reactive power control in Figure 5.14 exhibit identical characteristics. This raises a final assertion that the inner control loop is the most critical part affecting the small-signal stability of the proposed VSC system, while the outer loop controller does not have a major impact. In the next chapter, a quantitative method to assess the impact of the parameters on the critical eigenvalues is implemented to further validate the conclusion made through bifurcation analysis.

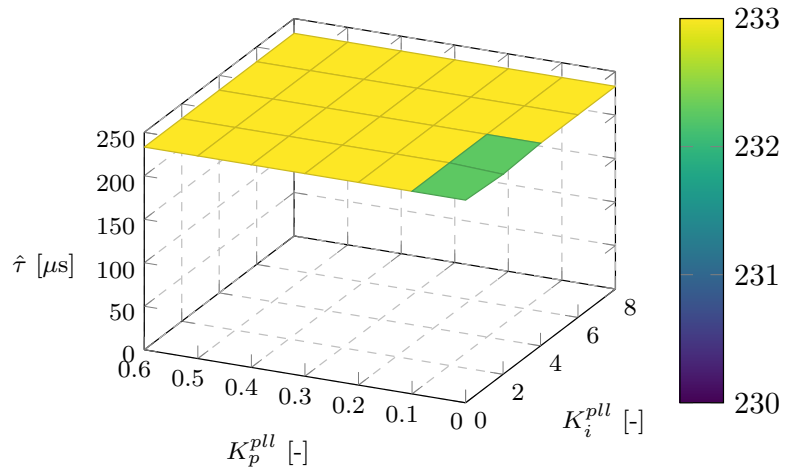


**Figure 5.14:** Stability Map on  $\hat{\tau} - K_p^{pl} - K_i^{pl}$  plane

## Chapter 6

# Parameter Sensitivity Analysis

As stated in [9] and [19], the parameter sensitivity of system eigenvalues is implemented to reveal the impact of the control parameters and further improve the stability and transient response of the system. First, a numerical definition is proposed below.

$$\mathbf{a}_{n,k} = \frac{\partial \lambda_n}{\partial \rho_k} = \frac{\Phi_n^T \frac{\partial A}{\partial \rho_k} \Psi_n}{\Phi_n^T \Psi_n} \quad (6.1)$$

The structure of equation 6.1 is virtually similar to the participation factor definition. Here  $\mathbf{a}_{n,k}$  represents the sensitivity of the  $n^{\text{th}}$  mode to the  $k^{\text{th}}$  parameter;  $A$  is the characteristic matrix of the proposed DDAE model, and  $\Phi_n^T$  and  $\Psi_n$  are right and left eigenvectors associated with eigenvalue  $\lambda_n$ , respectively.

If only the real value of the result  $\mathbf{a}_{n,k}$  is considered, the derivative of the real axis position of each eigenvalue over the changes of parameters is observed. The higher value of the real part of the result, the more distance will an eigenvalue moves to the horizontal positive direction per unit of parameter value increase. This will result in the conclusion that this specific eigenvalue is more sensitive towards the change of a particular controller parameter. Since the real value of the rightmost eigenvalue determines whether a system is stable or not, only the real part of the parameter sensitivity would be considered in the following analysis.

The results of parameter sensitivity analysis for two critical eigenvalues have been showcased in Figures 6.1 and 6.2. Both figures show that the parameter  $l_f$  has the highest parameter sensitivity. It should be noted that this parameter is the inductance of the LPF, which is predefined in the system and can not be altered after implementation. On the other hand, a significant sensitivity can be observed to the parameter  $K_{pc}$ , which represents the proportional gain parameter of the SRF current controller. Hence, a final conclusion is drawn from the above analysis that the SRF current controller has a predominant influence on the small-signal stability of the proposed VSC control system.

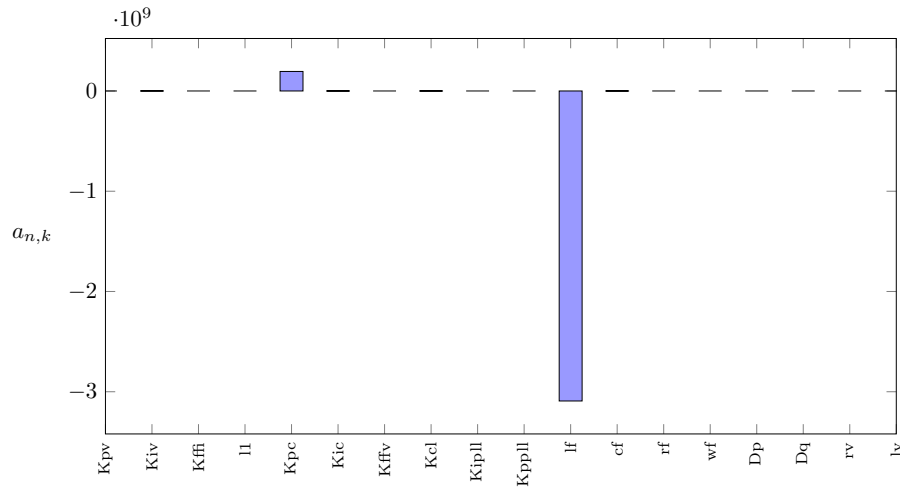


**Figure 6.1:** Parameter Sensitivity for critical eigenvalue  $\hat{\lambda} = 3.5697 \pm j6913.8684$

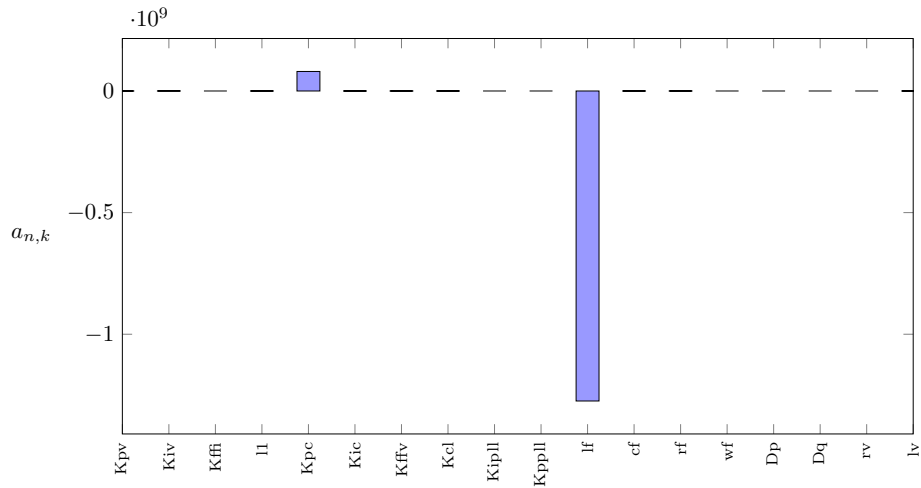


**Figure 6.2:** Parameter Sensitivity for critical eigenvalue  $\hat{\lambda} = 23.9151 \pm j7677.1995$

More specifically, the proportional gain parameter is the most sensitive variable to tune with respect to small-signal stability improvement of the system.

## Chapter 7

# Conclusion & Outlook

The main purpose of the project is to investigate the impact of time delay measurements signals to the small-signal stability of the proposed VSC system. Meanwhile, the existing DDAE model derived from the VSC control system has been extended to complete DDAE model, with the actual time delay signals have been properly represented in the mathematical format. Subsequently, two approximation techniques, named Chebyshev Discretization scheme and Padé Approximants have been implemented to obtain a subset of the transcendental equation solutions. Both single and multiple time-delay scenarios have been discussed as well as two other system configurations. Additionally, eigenvalue spectrums have been analyzed for all scenarios and compared. Furthermore, a two-dimensional and three-dimensional bifurcation analysis was conducted to provide a visualized overview of the impact of control parameters on the stability of the system. A quantitative calculation is also proposed at the end of the report to testify the hypothesis derived during the project.

The results have proved that both Chebyshev Discretization method and Padé Approximants technique are feasible to observe the system stability under time delays. Besides, the analysis confirms that the VSC system stability is most vulnerable to the measurement delays in the switching current at the output of the converter. Additionally, the SRF current controller has a predominant effect regarding the system resilience to time delays. These assumptions are testified through participation analysis and also parameter sensitivity analysis.

The DDAE model derived from this project could be further extended to incorporate the multi-converter model and analyze interoperability under time delays. Further research could be conducted to investigate the impact of signal delays in control setpoint inputs, e.g. AGC signals sent over long distances. Finally, a detailed study on a large-scale system, e.g. ENTSO-E grid, should be conducted.



# Bibliography

- [1] F. Milano, “Small-signal stability analysis of large power systems with inclusion of multiple delays,” *IEEE Transactions on Power Systems*, vol. 31, pp. 3257–3266, July 2016.
- [2] P. A. G. H. Uros Markovic, J. Vorwerk, “Stability analysis of converter control modes in low-inertia power systems,” in *2018 IEEE PES Innovative Smart Grid Technologies Conference*, 2018.
- [3] M. A. C. Z. Parmal Singh Solanki, Venkateswara Sarma Mallela, “Distributed generation to reduce carbon dioxide emissions: A case study for residential sector in oman,” *The Open Renewable Energy Journal*, 2010.
- [4] A. Ulbig, T. S. Borsche, and G. Andersson, “Impact of Low Rotational Inertia on Power System Stability and Operation,” *ArXiv e-prints*, Dec. 2013.
- [5] T. V. Van, K. Visscher, J. Diaz, V. Karapanos, A. Woyte, M. Albu, J. Bozelie, T. Loix, and D. Federenciuc, “Virtual synchronous generator: An element of future grids,” in *2010 IEEE PES Innovative Smart Grid Technologies Conference Europe (ISGT Europe)*, Oct 2010.
- [6] J. Driesen and K. Visscher, “Virtual synchronous generators,” in *2008 IEEE Power and Energy Society General Meeting - Conversion and Delivery of Electrical Energy in the 21st Century*, July 2008.
- [7] H. P. Beck and R. Hesse, “Virtual synchronous machine,” in *2007 9th International Conference on Electrical Power Quality and Utilisation*, Oct 2007.
- [8] S. D’Arco and J. A. Suul, “Virtual synchronous machines - classification of implementations and analysis of equivalence to droop controllers for microgrids,” in *2013 IEEE Grenoble Conference*, June 2013.
- [9] S. D’Arco, J. A. Suul, and O. B. Fosso, “Small-signal modelling and parametric sensitivity of a virtual synchronous machine,” in *2014 Power Systems Computation Conference*, Aug 2014.

- [10] D. Ramasubramanian, V. Vittal, and J. M. Undrill, "Transient stability analysis of an all converter interfaced generation wecc system," in *2016 Power Systems Computation Conference (PSCC)*, June 2016.
- [11] G. H. Uros Markovic, Petros Aristidou, "Stability performance of power electronic devices with time delays," in *PowerTech, 2017 IEEE Manchester*, pp. 1–6, 2017.
- [12] F. M. Vahid Bokharaie, Rifat Sipahi, "Small-signal stability analysis of delayed power system stabilizers," *2014 Power Systems Computation Conference*, 2014.
- [13] F. Milano and M. Anghel, "Impact of time delays on power system stability," *IEEE Transactions on Circuits and Systems I: Regular Papers*, vol. 59, pp. 889–900, April 2012.
- [14] W. Michiels and S.-I. Niculescu, "Stability and stabilization of time-delay systems (advances in design control)," in *Philadelphia, PA, USA: Society for Industrial and Applied Mathematics*, 2007.
- [15] X. K. Q. Cossart, F. Colas, "Model reduction of converters for the analysis of 100% power electronics transmission systems," *2018 IEEE International Conference on Industrial Technology (ICIT)*, 2018.
- [16] R. P. V. Konoval, "Participation factor in modal analysis of power systems stability," *Poznan University of Technology Academic journals*, 2016.
- [17] M. A. H. E. H. Abed and W. A. Hashlamoun, "Modal participation factors revisited: One definition replaced by two," *2009 American Control Conference*, June 2009.
- [18] M. A. H. W. A. Hashlamoun and E. H. Abed, "New results on modal participation factors: Revealing a previously unknown dichotomy," *IEEE Transactions on Automatic Control*, vol. 54, pp. 1439–1449, July 2009.
- [19] O. B. F. Salvatore DâArco, Jon Are Suul, "Small-signal modeling and parametric sensitivity of a virtual synchronous machine in islanded operation," *International Journal of Electrical Power and Energy Systems*, vol. 72, pp. 3–15, November 2015.